Physica E 147 (2023) 115611

Contents lists available at ScienceDirect

Physica E: Low-dimensional Systems and Nanostructures

journal homepage: www.elsevier.com/locate/physe

Single-wall pristine and Janus nanotubes based on post-transition metal chalcogenides. First-principles study

Andrei V. Bandura *, Dmitry D. Kuruch, Vitaly V. Porsev, Robert A. Evarestov

Quantum Chemistry Department, Saint-Petersburg State University7/9 Universitetskaya Nab., St. Petersburg, 199034, Russia

ARTICLE INFO

Keywords:
Janus monolayers
Janus nanotubes
Strain energy
Formation energy
Band gap
Elastic moduli

ABSTRACT

The first-principles simulations were performed to investigate the structure and properties of single-wall nanotubes constructed from the binary MX and mixed M_2XY, MLX_2 or MLXY (M, L = Ga, In, M ≠ L; X, Y= S, Se, Te, X ≠ Y) monolayers. Different types of parent monolayers, chirality and diameters of nanotubes have been considered. The simulation of Janus nanotubes based on post-transition metal chalcogenides has been performed for the first time. The stability of nanotubes was analyzed both with respect to bulk phases and with respect to monolayers. It is found that the monolayers of monoclinic phase may be preferable for folding of nanotubes in the case of GaTe. On the other hand, the Janus nanotubes possess the lower formation energy than their binary (pristine) counterparts if the heaver chalcogen atom is located on the external nanotube surface. The calculation of the electronic properties also indicates the promise of Janus nanotubes for photocatalytic applications. Young's and shear moduli, as well as Poisson ratios have been estimated for binary and mixed gallium chalcogenide nanotubes for the first time. Analysis of elastic properties of nanotubes based on gallium chalcogenides shows that they have lower rigidity than nanotubes based on transition metal chalcogenides.

1. Introduction

Post-transition metal chalcogenides (PTMC) form an extensive family of materials promising for use in various fields of science and technology. Among them, a special place is occupied by gallium and indium monochalcogenides MX (M = Ga, In; X = S, Se, Te), which are most often observed as layered bulk crystals [1].

In the last ten years, quite a lot of theoretical works have been published devoted to the calculation of the geometric, electronic, and phonon structures of bulk crystals and monolayers of gallium and indium monochalcogenides. Some publications [2–10] can be mentioned as examples.

The ultrathin films of Ga sulfides, selenides and tellurides, as well as In selenides have shown great potential in electronics and optoelectronics [1]. Taking into account the achieved experience in the application of monolayers of transition metal dichalcogenides (TMC) in the field of nanoelectronics (e.g. for the design of diode and transistor devices [11,12]) one should expect an accelerated growth of applications in which nanolayers of PTMC may be used. Particularly, GaSe crystal exhibits strong nonlinear optical properties and finds application in laser optics as a material for the fast frequency conversion [3,13,14]. GaTe crystals were found to be suitable for using as high energy radiation detectors [15]. Furthermore, some indium monochalcogenides (for instance, InSe) proved to be promising for converting solar energy into electricity [16]. Additionally, electrochemical studies [17] provide insight into the extensive electrocatalytic performances towards hydrogen evolution, oxygen evolution and oxygen reduction reaction of layered indium chalcogenides.

Quasi two-dimensional layered materials have gained a lot of attention when they have been reduced to one or few atomic layers. Such nanolayers can be obtained, for example, by the chemical vapor deposition (GaS [18]; GaSe [19]), the growth-etching-regrowth process (GaSe [20]), the phase-controlled synthesis on the MoS_2 substrate (GaTe [21]), or the physical vapor deposition method (InSe [22]). Another approach is the shear-force milling [23], which proved to be an effective method for the exfoliation of indium and gallium chalcogenides (GaS, GaSe, GaTe, InSe, InTe). It was shown [23] that exfoliated InSe can find application in the gas sensing due to its high sensitivity and selectivity. On the other hand, it was demonstrated [5,19,24] that nanosheet-based GaS and GaTe can be used as highly sensitive photodetectors. Inherent electrochemical properties of nanomaterials based on PTMC are discussed in the recent work [25]. These properties could potentially affect

* Corresponding author.
E-mail address: andrei@ab1955.spb.edu (A.V. Bandura).

https://doi.org/10.1016/j.physe.2022.115611
Received 6 May 2022; Received in revised form 13 October 2022; Accepted 7 December 2022
Available online 8 December 2022

the PTMC efficiency when applied as electrode materials. The relative stability of group III metal monolayer monochalcogenides as well as their suitability for photocatalytic water splitting, have also been modeled from the first principles [2].

Recently, there has been an explosive growth of interest in the so-called Janus monolayers, which have different composition of boundary surfaces. The design principles, synthesis, and the properties of chalcogenide-based Janus layers are discussed in the recent paper [26] . Although no synthesis of Janus PTMC has yet been reported, similar systems have been successfully synthesized for TMC. For example, a WSSe monolayer was fabricated by implanting Se atoms into a WS_2 monolayer using the pulsed plasma laser ablation technique [27], while a MoSSe monolayer was synthesized using a modified chemical vapor deposition method as a result of selenization of the MoS_2 monolayer [28] or sulfurization of the $MoSe_2$ monolayer [29].

Guo et al. [30] were evidently the first to design all possible Janus monolayers from group III metal monochalcogenides. The considered Janus structures can be divided into two groups: M_2XY (M = Ga, In; X, Y = S, Se, Te; $X \neq Y$) and MLX_2 (M, L = Ga, In; $M \neq L$, X = S, Se, Te). The calculations [30] confirmed that the Janus structures are dynamically and thermodynamically stable. The authors of this study [30] found that the monolayers under consideration have a band gap in the range of 0.89–2.03 eV, which is lower than that of pristine (binary) monolayers. Moreover, for Ga_2STe, Ga_2SeTe, In_2STe, and In_2SeTe monolayers, the band gap turns out to be direct. It has been established that these monolayers exhibit piezoelectric properties, which makes it possible to consider them as promising materials for piezoelectric sensors and nanogenerators. In the work of Kandemir and Sahin [31], the strain dependence of the electronic properties of In_2SSe Janus monolayers were investigated, and it was shown that Janus In_2SSe monolayer has a direct band gap. The dependence of the electronic and optical properties of a $GaInS_2$ monolayer on strain and electric field have been also studied by Betal et al. [32] using density functional theory (DFT) and the time-dependent density functional perturbation theory. It was found that at a compressive strain of 4%, the band gap of the material changes from indirect to direct.

From the studies carried out, it becomes clear that Janus-type nanolayers expand the area of potential use, showing properties that are not found in binary systems. For example, the use of a Janus WSeTe monolayer instead of WSe_2 or WTe_2 monolayers provides improved performance for atomic-thin Schottky-barrier field-effect transistors [12].

In the work of Bui et al. [33] the optical and electronic properties of Janus monolayers based on gallium chalcogenides have been analyzed. The authors concluded that the combination of optical and electronic properties of Ga_2SSe, Ga_2STe, and Ga_2SeTe monolayers provides great opportunities for their use in UV radiation detectors and photovoltaic absorbers. On the other hand, Pang et al. [34] have shown that Janus group-III chalcogenide monolayers (Ga_2SSe, In_2SSe) have a high selectivity for the adsorption of polar gas molecules and, therefore, can be used as highly sensitive gas sensing materials.

Bai et al. [35] suggested the likely use of single-layer Janus PTMC as photocatalysts. The authors found that the position of the Janus PTMC band edge is suitable for photocatalytic water splitting, possibly with the exception of Ga_2STe, in which the valence band edge is above the oxidation potential. In addition, the direct band gap of Ga_2SeTe, In_2STe and In_2SeTe is favorable for photocatalysis. A similar study by Huang et al. [36] not only proved the efficient photocatalytic performance of 2D M_2XTe (M = Ga, In; X = S, Se) monolayers, but also proposed an approach to tuning the band gap of 2D photocatalysts by selecting specific Janus structures. Linear and circular photogalvanic effects in Janus monolayer In_2SSe have been studied by non-equilibrium Green's function technique and DFT in the work of Wang et al. [37]. The obtained results show that the In_2SSe Janus monolayer is a favorable material for visible light solar cells. The analogous study has been done for the In_2SeTe monolayer by Zhao et al. [38]. The data revealed indicate that the photocurrent of In_2SeTe solar cells can be comparable with thin-film silicon devices.

The layered structure of PTMC, as well as the possibility of forming free nanolayers makes it very probable that quasi one-dimensional nanoobjects such as nanotubes (NTs) can be obtained. Indeed, nanotubes based on gallium sulfide and selenide have actually been synthesized [39–41]. Firstly, a simple method was proposed for obtaining multiwalled GaS nanotubes by annealing a lamellar precursor prepared from sulfur and gallium powders in gaseous Ar [39]. Almost simultaneously, the multilayer GaS and GaSe nanotubes have been created by exfoliation under the action of laser irradiation or thermal treatment of bulk chalcogenide powders [40]. Ten years later, the amine-templated gallium chalcogenide nanotubes were synthesized [41] through the reaction of gallium (III) acetylacetonate and chalcogen (sulfur or selenium) using a mixture of amines as a solvent. In addition, GaS thin films were generated [42] by atomic layer deposition onto single-wall carbon nanotubes. The resulting composite material has proven to be a highly efficient anode for lithium-ion batteries [42].

To the best of our knowledge, there are no works on the preparation of nanotubes based on gallium tellurides or indium monochalcogenides. Only a few reports on the synthesis of nanotubes based on indium (III) sulfide have been published [43,44].

Despite the rather large amount of experimental data, theoretical studies of nanotubes based on gallium and indium chalcogenides are limited to a several publications. First of all, one should note the studies of single-wall GaS nanotubes carried out by Seifert and his co-workers [45,46] in the framework of the semi-empirical density functional theory tight-binding (DFTB) method [47]. The first ab initio calculation was performed by Côté et al. [48] for GaSe single-wall nanotube (SWNT) in the local density approximation. A comparison of the structure and stability of GaS and GaSe nanotubes was carried out by Karpov et al. using the PBE0 exchange correlation functional (containing 13% Hartree-Fock exchange) [49]. In this work, it is shown that the strain energy of the nanotubes of gallium selenide is higher than that of gallium sulfide at the same diameters. Nevertheless, the strain energies of nanotubes of the same composition and diameter, but of different chirality, practically do not differ. Only one theoretical study was devoted to InS nanotubes [50]. In this work, the structure and stability of single- and double-walled nanotubes were analyzed. It has also been shown that some InS nanotubes are promising for photocatalytic water splitting in the visible region of the light spectrum.

It should also be noted that Janus nanotubes exist in nature. The mineral imogolite $Al_2SiO_3(OH)_4$ [51] includes single-wall Janus nanotubes, while the minerals halloysite $Al_2Si_2O_5(OH)_4$ [52] and chrysotile $Mg_3Si_2O_5(OH)_4$ [53] form multi-walled Janus nanotubes. Single-wall imogolite Janus nanotubes were first synthesized almost half a century ago [54] by heating weakly acidic dilute solutions containing hydroxyaluminium orthosilicate complexes. By this method, a fibrous polymer was obtained, each fiber of which consisted of Janus nanotubes with an outer diameter of about 2.2 nm and an inner diameter of 1.0 nm. The selective etching method was used to create a new modification of multi-walled halloysite Janus nanotubes [55].

No other single- or multi-walled Janus-NTs were found experimentally. Particularly, the Janus nanotubes have not been synthesized for either TMC or PTMC. However, there are a lot of theoretical studies of Janus SWNTs based on transition metal dichalcogenides (see, for example, Refs. [56–58] and references therein). As pointed out by Bölle et al. [58], the formation of the Janus SWNTs should be driven by an intrinsic self-rolling force existing in asymmetric 2D Janus sheets due to a lattice mismatch between inner and outer atomic planes.

No reports on PTMC Janus nanotubes have been published, except for our previous study [59] in which the first-principles calculations were used to provide the benchmark systems for classical force-field fitting.

The present first-principles study is aimed at comparing the properties of various single-wall nanotubes composed of layers of gallium

and indium monochalcogenides with different structures. Analysis of the relative stability of monolayers is carried out at the preliminary stage of our study. The structure, stability, electronic and elastic properties of a large number of pristine and Janus nanotubes are found and discussed by us. The results obtained for Janus nanotubes, as well as for pristine GaTe, InSe, and InTe-based nanotubes, are presented for the first time. The possibility of tuning of the electronic properties of PTMC nanotubes for photocatalytic water splitting is analyzed.

This article is organized as follows. In the "Computational details" section, we describe the methods used in this study. In two following sections, "Slab models" and "Nanotube models" we briefly consider the structure and properties of 2D monolayers originated from the various bulk phases, as well as the models used to design the nanotubes from the considered layers. In the "Results and discussion section", we present and discuss the results obtained for the structure, stability, electronic and elastic properties of pristine and Janus nanotubes. The main results of our research are presented in the "Conclusion" section.

2. Computational details

Our calculations were performed within the framework of the periodic DFT using the hybrid exchange-correlation functional M06 [60]. The basis set of localized atomic orbitals, implemented in the CRYSTAL17 [61,62] computer code, was used to expand the crystalline orbitals. The all-electron basis pob_DZVP_rev2 [63] was applied for Ga, S and Se atoms. To describe the interaction of core and valence electrons in and Te atoms, we used the m-pVDZ-PP_Heyd [64] basis set and the corresponding effective core pseudopotentials. The subvalent 4*s*-, 4*p*- and 4*d*-shells have been explicitly included for the In and Te atoms.

When calculating the direct lattice sums of one-electron and two-electron Coulomb and exchange integrals, the tight thresholds [62] of 10^{-8}, 10^{-8}, 10^{-8}, 10^{-9} and 10^{-18} were used. The Brillouin zone of the MX bulk crystals with space group (SG) 194, $P6_3/mmc$, was sampled using a Monkhorst-Pack [65] 16 × 16 × 4 **k**-point grid. In other cases, the grid in the reciprocal space was set to be inversely proportional to the respective cell constants to ensure roughly the same density in the **k**-point sampling mesh.

To take into account the dispersion contributions to the van der Waals (vdW) interactions between MX layers, we applied the zero-damping approach DFT-D3 [66] implemented in the CRYSTAL17 code [62]. Following this approach, the dispersion correction D3 (DC) includes damped atom-atom pairwise empirical term added to the Kohn-Sham DFT total energies. The default values built into CRYSTAL17 code [62] were used for DC parameters.

The built-in capabilities of the CRYSTAL17 [62] code were used to create the initial structures of single-wall nanotubes. The lattice parameters and positions of all atoms in the considered systems were optimized while searching for the most stable structures.

The described computational approach has been tested on the properties of the stable bulk phases of gallium and indium chalcogenides. Comparison of the results obtained with the available experimental data shows a good agreement of both structural and electronic properties (Table 1). It should be noted that bulk monochalcogenide phases have been the subjects of a recent theoretical study [10] using plane wave DFT, which was performed to determine the relative energies of competing polytypes of bulk layered hexagonal gallium and indium chalcogenides. The reported [10] accuracy of reproducing the experimental data for the lattice parameters of the GaS, GaSe, and InSe hexagonal phases is approximately the same as in the present work.

3. Slab models

Most of the stable bulk phases of gallium and indium chalcogenides consist of layers weakly interacting with each other via vdW forces. The only exceptions are the modifications of indium sulfide and telluride, which do not show layering and occur in the orthorhombic and tetragonal phases (Table 1) at ambient conditions.

To investigate the relative stability of various nanotubes and their precursor monolayers, we considered the same set of structures based on experimentally observed modifications of layered bulks. In this set, we included hexagonal, trigonal, and monoclinic structures. Various hexagonal polytypes are known for the stable phases of GaS, GaSe, and InSe (see Table 1), the monoclinic ($C2/m$) phase corresponds to the low-temperature modification of GaTe, and the rhombohedral polymorph, R–$3m$, is experimentally found for GaS [78]. This choice is due, on the one hand, to the real existence of the phases under consideration, and, on the other hand, to the presence of the main types of monolayers inherent in the chalcogenides of group IIIA metals.

The stability of various monolayers can be estimated using their formation energy from a certain reference state. In this work, the formation energy of monolayers E_{form} is calculated by the following expression:

$$E^{\text{MX}}_{\text{form}} = E^{\text{MX}}_{\text{mono}} \Big/ N^{\text{MX}}_{\text{mono}} - E^{\text{MX}}_{\text{bulk}} \Big/ N^{\text{MX}}_{\text{bulk}}, \quad (1)$$

where $E^{\text{MX}}_{\text{mono}}$ is the monolayer unit cell (UC) energy, $E^{\text{MX}}_{\text{bulk}}$ is the UC energy of the most stable bulk phase of the MX crystal, $N^{\text{MX}}_{\text{mono}}$ and $N^{\text{MX}}_{\text{mono}}$ are the corresponding numbers of MX formula units. The calculated difference in total energy between hypothetical substances and the stable phases (see Table 1) of the same composition allows us to assess the fundamental possibility of their real existence. Monolayers of bulk crystals with SG 194 and SG 166 were cleaved parallel to (001) atomic plane, while monolayers from the bulk crystals with SG 12 were cleaved parallel to (−201) atomic plane. The first two monolayers exhibit hexagonal morphology and consist of two M-planes (covalently bonded with each other) sandwiched between two X-planes (Fig. 1a and b). The

Table 1
Calculated properties[a,b] of the most stable bulk MX phases (M = Ga, In; X = S, Se, Te).

Crystal	SG	*a* (Å)	*b* (Å)	*c* (Å)	*β* (°)	Band gap, E_{gap} (eV)	direct/indirect band gap
GaS	194, $P6_3/mmc$	3.608	3.608	15.524		3.06	i
		(3.585)	(3.585)	(15.500)		(3.1 [73])	
GaSe	187, P–$6m2$	3.763	3.763	15.984		2.58	i
		(3.743)	(3.743)	(15.919)		(2.1 [74])	
GaTe	12, $C2/m$	17.919	4.110	10.694	106.3	2.31	i
		(17.404)	(4.077)	(10.456)	(104.4)	(1.7 [75])	
InS	58, $Pnnm$	4.525	10.898	3.990		2.14	i
		(4.453)	(10.650)	(3.945)		(2.1 [76])	
InSe	160, $R3m$	4.021	4.021	25.275		1.66	d
		(4.000)	(4.000)	(24.950)		(1.2 [77])	
InTe	140, $I4/mcm$	8.822	8.822	7.277		1.15	d
		(8.454)	(8.454)	(7.152)		(1.2 [75])	

[a] Experimental values are given in parentheses.
[b] Experimental lattice parameters *a*, *b*, *c*, and *β* are taken from following works [67] for GaS, [68] for GaSe, [69] for GaTe, [70] for InS, [71] for InSe, and [72] for InTe.

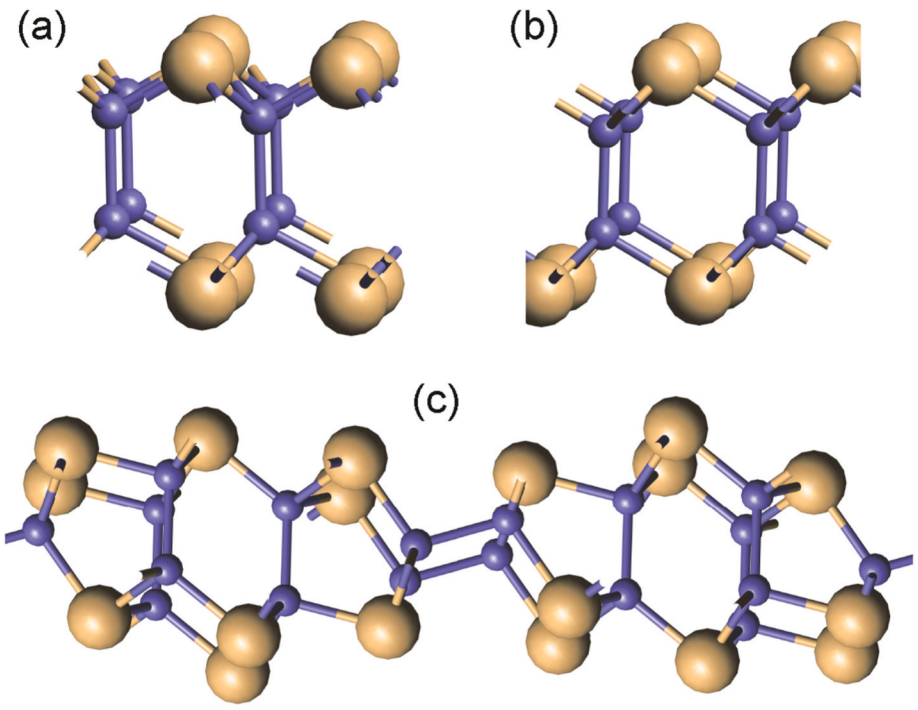

Fig. 1. Structure of monolayers cut from bulk MX phases (M = Ga, In; X = S, Se, Te) with SG 194 (001) (a), SG 166 (001) (b), and SG 12 (−201) (c). (Colors in online version: small blue spheres – M atoms, large beige spheres – X atoms.)

corresponding 2D layer groups (LGs) are 78 (*p*–6*m*2) and 72 (*p*–3*m*1).

Monolayers isolated from the monoclinic phases (SG 12) are composed of rigid M_6X_6 chains parallel to [010] direction in conventional centered rectangular *c*12/*m*1 (LG 18) cell, which are connected by M–M bonds between metal atoms laying in perpendicular planes (see Fig. 1c). This geometry provides a large flexibility of the monolayers in [100] direction (see next section below).

Table 2
Calculated properties of MX monolayers (M = Ga, In; X = S, Se, Te).

Crystal	LG	Parent bulk SG	Lattice parameter, *a* (*b*[a]) (Å)	Formation energy, E_{form} (kJ mol^{-1})	Band gap, E_{gap} (eV)	direct/ indirect band gap
GaS	18	12	3.606 (21.491)	23.2	4.18	i
	72	166	3.620	15.0	4.25	i
	78	194	3.611	14.5	4.09	i
GaSe	18	12	3.755 (22.121)	21.4	3.77	i
	72	166	3.767	14.2	3.95	i
	78	194	3.758	13.7	3.87	i
GaTe	18	12	4.088 (23.557)	15.7	2.76	d
	72	166	4.092	13.5	2.83	i
	78	194	4.074	13.6	2.88	i
InS	18	12	3.868 (23.821)	36.5	3.07	i
	72	166	3.887	24.4	3.17	i
	78	194	3.883	23.9	3.22	i
InSe	18	12	4.003 (24.339)	28.4	3.05	i
	72	166	4.018	18.8	3.13	i
	78	194	4.014	17.9	3.20	i
InTe	18	12	4.313 (25.327)	22.3	2.50	d
	72	166	4.318	20.3	2.71	i
	78	194	4.310	19.7	2.74	i

[a] The lattice parameters *a* and *b* (in parentheses) of the conventional rectangular UC are given for monolayers cleaved from the monoclinic *C*2/*m* phase.

The data presented in Table 2 demonstrate close calculated values of the lattice parameters *a*, as well as electron band gaps E_{gap} for monolayers of the same composition cleaved from different bulk phases. The monolayer formation energies computed relative to the stable bulk phases increase in the following order: *p*–6*m*2 ≤ *p*–3*m*1 < *c*12/*m*1. The formation energies of the monolayers cleaved from different phases of the gallium chalcogenides with the same symmetry are quite close, except that the GaTe base-centered rectangular layer reveals noticeably greater stability compared to similar GaS and GaSe structures. In this case the most stable phase is monoclinic with the SG 12, therefore, the difference in the formation energy of different monolayers is small. Indium chalcogenide monolayers demonstrate one and a half times lower stability, and the minimal formation energy is observed for hexagonal InSe layers.

The structure and stability of mixed (Janus) monolayers with composition MLXY (M, L = Ga, In; X, Y = S, Te) have also been studied to provide the parent layers for Janus NTs rolling up. These monolayers have been constructed from binary M_2X_2 precursors by replacing a chalcogen or/and metal atom in one/two adjacent planes on one side of the layer. This ensures that for the MLXY monolayer, metal M is chemically bonded to chalcogen X, and metal L is chemically bonded to

Table 3
Calculated properties of Janus MLXY monolayers (M, L = Ga, In; X, Y = S, Te) with symmetry of layer group 69 (*p*3*m*1).

Crystal	SG of parent binary bulk phases	Lattice parameter, *a* (Å)	Formation energy, E_{form} (kJ mol^{-1})	Band gap, E_{gap} (eV)	direct/ indirect band gap
Ga_2STe	194	3.858	27.8	2.52	d
	166	3.871	27.8	2.53	d
In_2STe	194	4.098	31.1	2.08	d
	166	4.104	31.6	2.07	d
$GaInS_2$	194	3.748	25.4	3.53	i
$GaInTe_2$	194	4.185	20.6	2.53	i
GaInSTe	194	3.964	45.8	1.35	d

chalcogen Y.

The main calculation results are presented in Table 3. The formation energy of Janus monolayers is calculated using the following formula:

$$E_{\text{form}}^{\text{MLXY}} = \frac{1}{2}\left(E_{\text{mono}}^{\text{MLXY}}/N_{\text{mono}}^{\text{MLXY}} - E_{\text{bulk}}^{\text{MX}}/N_{\text{bulk}}^{\text{MX}} - E_{\text{bulk}}^{\text{LY}}/N_{\text{bulk}}^{\text{LY}}\right), \quad (2)$$

where $E_{\text{mono}}^{\text{MLXY}}$ and $N_{\text{mono}}^{\text{MLXY}}$ are the energy and the number of MLXY formula units for the monolayer unit cell, correspondingly, and the factor 1/2 is ensures the same energy scale as has been used for pristine monolayers. The data of the first 4 rows of Table 3 confirm that monolayers with parent SG 166 have similar properties as monolayers with parent SG 194. It is also interesting to note, that the lattice parameter a of Janus monolayer can be well estimated as the arithmetic mean between the lattice parameters of the parent binary monolayers. For instance: a (GaInSTe) = 3.964 Å, while 1/2 [a(GaS)+a(InTe)] = 3.961 Å. From the data in Table 3 we can conclude that the Janus monolayers are significantly less stable than the parent pristine ones. This is most clearly seen for the GaInSTe monolayer, whose formation energy is almost three times higher than the average formation energy of GaS and InTe (17.1 kJ mol^{-1}). The reason for this, obviously, lies in the tension that occurs between the "upper" and "lower" half-layers, which should have different cell constants in the parent pristine monolayers.

The data in Table 2 show that the energy band gap of binary indium chalcogenide monolayers is lower than E_{gap} of the corresponding gallium chalcogenide monolayers and also decreases with increasing of the mass of the chalcogenide atom: MS ≈ MSe > MTe. In the most of binary monolayers the band gap possesses the indirect character. In the case of Janus chalcogenides, the band gap turns out to be smaller than might be expected based on the values for the parent binary phases. As a result, the maximum E_{gap} = 4.2 eV was found for the GaS monolayers, and the minimum E_{gap} = 1.4 eV – for the GaInSTe monolayer. The band gap is direct for all Janus monolayers except for $GaInS_2$ and $GaInTe_2$.

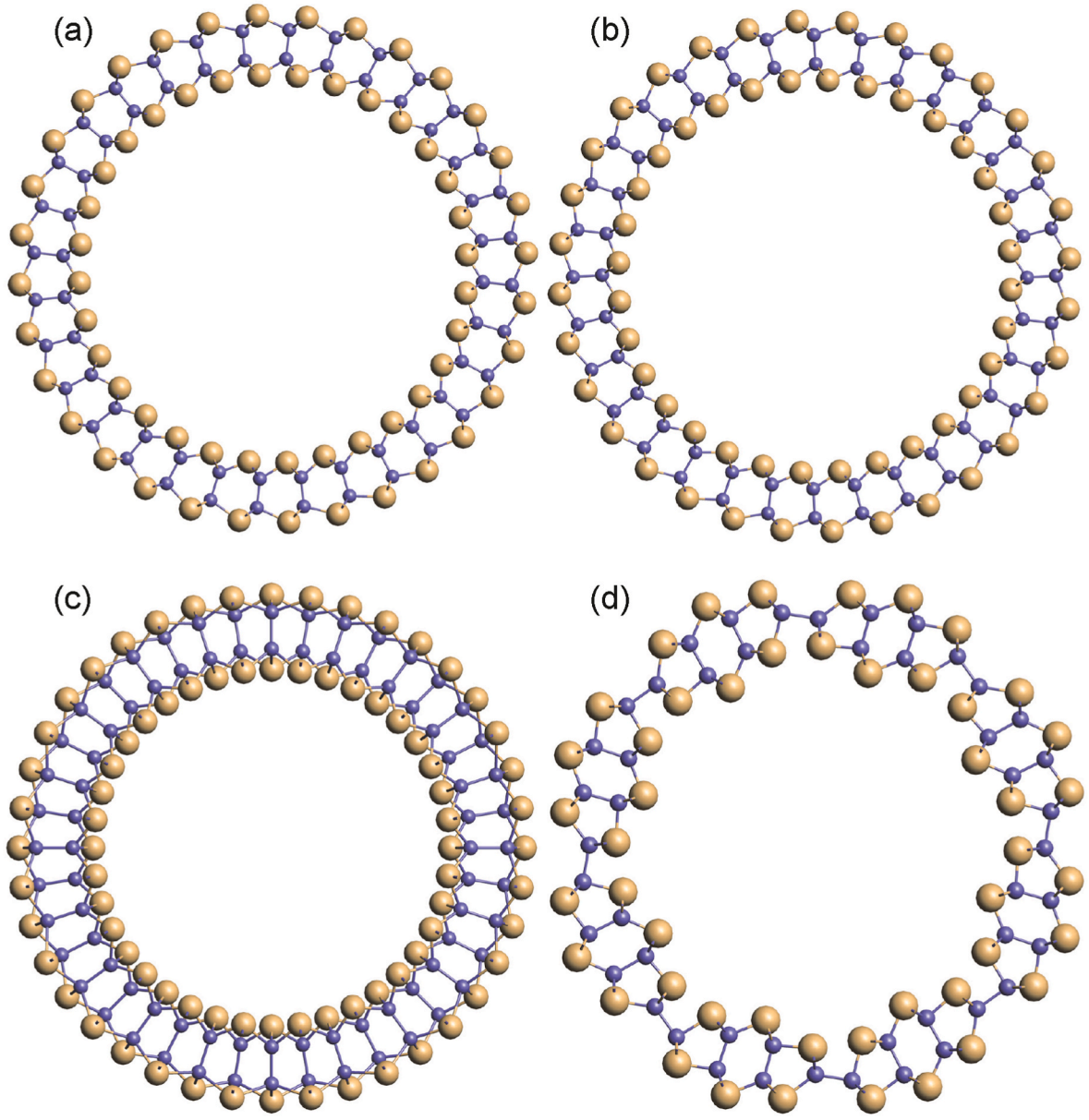

Fig. 2. Cross-sectional view of optimized structure of NTs folded from the monolayers cut: (a) from the phase of SG 194 with chirality (16, 16); (b) from the phase of SG 166 with chirality (16, 16); (c) from the phase of SG 194 with chirality (20, 0); and (d) from the phase of SG 12 with chirality (4, 4). (Colors in online version: small blue spheres are gallium or indium atoms, large beige spheres are sulfur or tellurium atoms.)

4. Nanotube models

The initial structure of 1D periodic nanotubes can be obtained as a result of the so-called single layer folding [79–81], which means the construction of cylindrical surfaces of nanotubes by rolling up two-periodic (2D) crystalline layers. In this approach, two vectors must be defined for a specific chirality of the nanotube (n_1, n_2): the rolling vector **R** and the translation vector **L**. The vector **R** determines the chirality and diameter of the nanotube, passing into the circumference of the cylindrical surface when the nanotube is rolled up. Vector **L** is the smallest two-dimensional translation vector normal to **R**, which provides the one-dimensional periodicity along the nanotube axis. In the basis ($\mathbf{a}_1$, $\mathbf{a}_2$) of the layer UC, both vectors are represented by integer coefficients: $\mathbf{R} = n_1\mathbf{a}_1+n_2\mathbf{a}_2$, $\mathbf{L} = l_1\mathbf{a}_1+l_2\mathbf{a}_2$. For a given symmetry of the 2D layer, the possible types of NT chirality (n_1, n_2) are uniquely determined by the orthogonality condition between **R** and **L** [80].

As has been shown in the previous section, the hexagonal $P6_3/mmc$ (SG 194) and trigonal R–3m (SG 166) phases of MX crystals provide the hexagonal (001) monolayers, which after rolling up [80] can form zigzag (n, 0) and armchair (n, n) achiral SWNTs (see Fig. 2a, b and c). The zigzag nanotubes belong to the line group family (LGF) 8 ($L(2n)_nmc$), while the armchair nanotubes belong to the LGF 4 ($L(2n)_n/m$).

According to Damnjanović et al. [80] there are two possible chiralities, (n, n) and (n, $-n$), for periodic NTs rolled up from the centered rectangular ($c12/m1$) 2D layers. Note that the chirality indices in this case are defined [80] with respect to a primitive rhombic cell spanned on the vectors **a'** and **b'** with $a' = b'$ and $\gamma' \neq 90°$. If we use the basis vectors **a** and **b** of the conventional rectangular cell ($a \neq b$ and $\gamma = 90°$), the (n, n) and (n, $-n$) chiralities defined with primitive basis should be rewritten as (n, 0) and (0, n), accordingly. The folding of monolayers in [100] direction corresponds to (n, 0) NT chirality in conventional basis or (n, n) NT chirality in primitive basis. Due to the above mentioned flexibility, the formation energy of (n, 0) NTs predicted to be much less than that of (0, m) NTs of the similar diameter. Additionally, in the case of the (−201) layers from the monoclinic phase, the length of the **a** vector approximately 6 times larger than length of the **b** vector ($a \approx 6b$). This means that for NTs of similar diameters the 1D (0, m) unit cell consists of 6 times more atoms than (n, 0) unit cell. These are the two reasons why only (n, 0) chirality (see Fig. 2d) has been chosen for the study of NTs generated from the layers of monoclinic phases. Below we will use the primitive UC notation (n, n) for this chirality. The n values have been varied from 3 to 10 to provide the NT diameters in the range from 20 to 80 Å. According to 1D classification [80] these nanotubes belong to the LGF 4 ($L(2n)_n/m$).

Janus nanotubes have been generated from the mixed nanolayers MLXY (M, L = Ga, In; X, Y = S, Te) in the same way as the pristine SWNTs. However, only structures with larger atoms (Te and/or In) in the outer NT shells were considered. The transition from pristine to Janus nanotubes does not change their LGF.

5. Results and discussion

5.1. Stability of nanotubes generated from the layers of binary chalcogenides

In this study, we performed DFT calculations of SWNTs folded from monolayers that were isolated from the layered chalcogenide phases discussed above. The dependence of the calculated properties on NT diameter and chirality has been investigated. The interval of the NT diameters d_{NT} studied varies from approximately 20 to 80 Å. The average d_{NT} value was estimated as the sum of the distances from the NT axis to the nearest (R_{min}) and the most distant (R_{max}) chalcogen atoms. There were prepared and optimized six (n, n) and four (n, 0) SWNTs folded from (001) layers of the hexagonal (SG 194) and trigonal (SG 166) phases, and five (n, n) SWNTs folded from (−201) layers of the monoclinic (SG 12) phase. Generally, all considered NTs keep the initial symmetry during the geometry optimization procedure. The optimized parameters of the nanotubes are given in Supplementary Material (SM), Table S1.

The stability of binary NTs is traditionally measured by the so called strain energy, E_{str},

$$E_{str}^{MX} = E_{NT}^{MX}/N_{NT}^{MX} - E_{mono}^{MX}/N_{mono}^{MX}, \quad (3)$$

where E_{NT}^{MX} is the total energy of NT cell, while N_{NT}^{MX} is the corresponding numbers of MX formula units. Since the free-standing monolayers do not really exist for all the considered chalcogenides, the energy of formation from bulk crystals, E_{form},

$$E_{form}^{MX}(NT) = E_{NT}^{MX}/N_{NT}^{MX} - E_{bulk}^{MX}/N_{bulk}^{MX} \quad (4)$$

is perhaps a more practical criterion for the stability of nanotubes. Also, the calculation of formation energies relative to the most stable bulk phases provides a more correct comparison between nanotubes of different composition.

Looking ahead, it should be noted that the calculated properties of NTs folded from the hexagonal layers with symmetry p–$6m2$ (LG 78) and p–$3m1$ (LG 72) practically do not differ. Moreover, the strain E_{str} and formation E_{form} energies of the (n, n) and (n, 0) NTs with hexagonal morphology are very close at equal diameters. This can be clearly seen in Fig. 3, where we compare the dependence of E_{str} and E_{form} on the GaS nanotube diameter. Therefore, below we mainly discuss the results obtained for NTs of the first type (folded from the layers of LG 78) with chirality (n, n). Fig. 3 also demonstrates that the stability of NTs with rectangular morphology is less dependent on the NT diameter than that of NTs with hexagonal morphology. The strain energy of SWNTs generated from monoclinic phase layers is considerably lower than that of SWNTs generated from hexagonal phase layers. The difference in formation energy is smaller than the difference in strain energy due to the relatively high formation energy of the rectangular layers. Nevertheless, one can see that SWNTs generated from monoclinic phase layers are more favorable at small diameters ($d_{NT} < 50$ Å). These circumstances are obviously related to the great flexibility of the rectangular layers.

In Fig. 4 we compare the diameter dependence of both the strain E_{str} and formation E_{form} energy for selected SWNTs of the chirality (n, n). It can be seen in Fig. 4a that at similar diameters the values of the strain energy of hexagonal NTs are close for all Ga and In chalcogenides. In all cases considered, the strain energy tends to zero with an increase of the NT diameter, since the total energy of the NT (per formula unit) tends to the corresponding energy of the monolayer. The curves for the E_{str} of In chalcogenides are practically undistinguishable and lie below the curves for Ga chalcogenides which arranged in the following order: GaS < GaSe < GaTe. However, as regards the energy of formation, the order of these curves is different. At a given NT diameter, the formation energies of Ga chalcogenides are lower than the formation energies of In chalcogenides, with indium sulfide exhibiting the maximum values. Finally, E_{form} disposes in the sequence: GaS < GaSe ≈ GaTe < InSe < InTe < InS. The dissimilarity in the behavior of E_{form} and E_{str} is obviously due to the different structure of parent bulks and, as a result, unequal stability of hexagonal monolayers. Thus, the monolayers of InS and InTe have a sufficiently large formation energy from the stable non-hexagonal phases, that leads to relatively low stain energy and relatively high formation energy. InSe NTs are the most stable among indium monochalcogenide NTs, which is also due to the fact that the hexagonal (SG 194) phase is the most stable bulk phase for the InSe crystal.

A somewhat different picture is observed for the stability of nanotubes rolled up from layers of monoclinic phases. First of all, the strain energy of such NTs is relatively low and does not exceed 5 kJ mol^{-1} for diameters greater than 30 Å (Fig. 4c). Moreover, in this region of diameters, the negative strain energy is observed in the case of InS and InSe nanotubes as a consequence of the relatively large positive formation energy of the initial monolayers. The formation energy of NTs

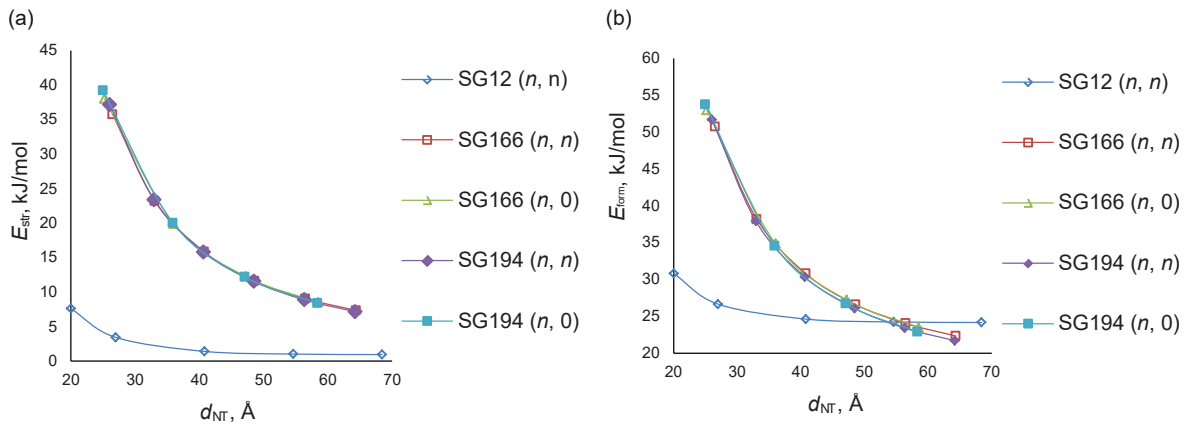

Fig. 3. Comparison of strain (a) and formation (b) energies of different types of SWNTs folded from layers of GaS.

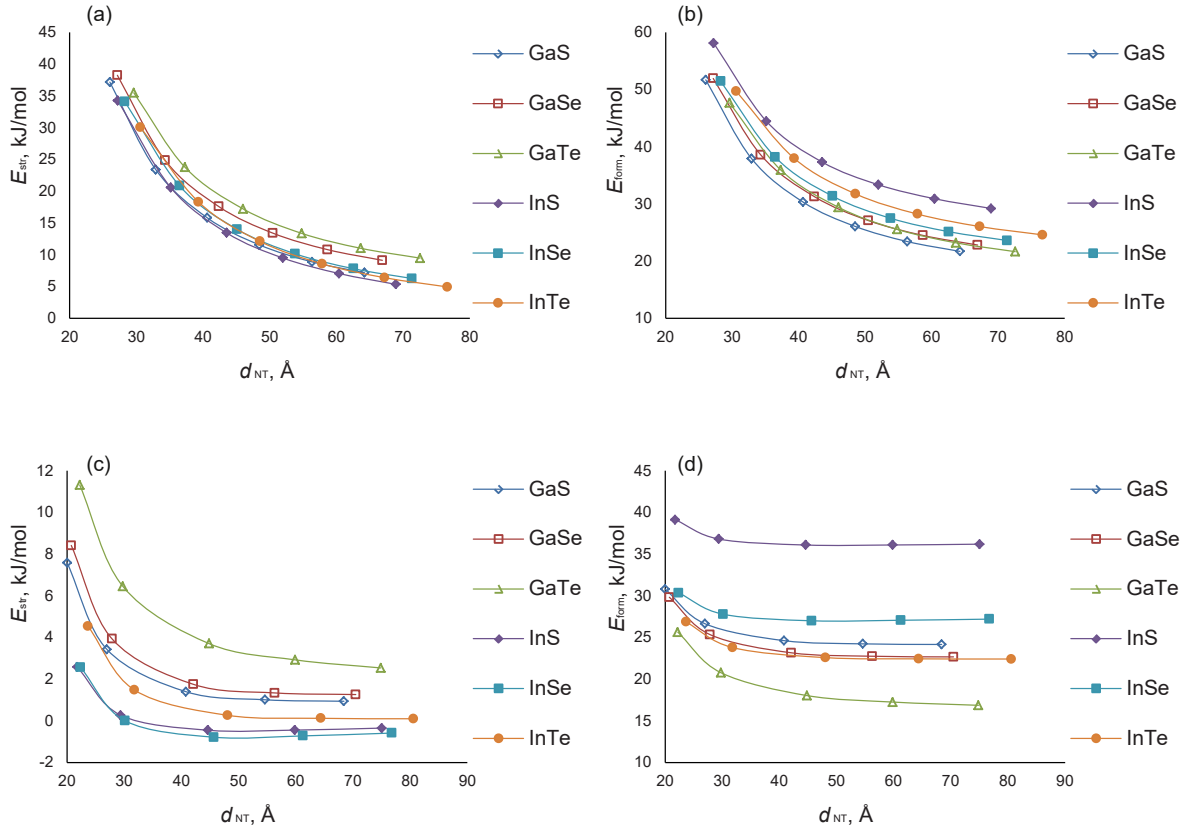

Fig. 4. Dependence of strain energy E_{str} (a, c) and formation energy E_{form} (b, d) on average tube diameter d_{NT} for MX armchair NTs (M = Ga, In; X = S, Se, Te) folded from layers of the hexagonal (SG 194, a, b) and monoclinic (SG 12, c, d) phases.

with rectangular morphology, calculated with respect to the stable bulk phases, increases in the following order: GaTe < InTe ≈ GaSe < GaS < InSe < InS. Thus, GaTe NTs are the most stable among all SWNTs considered, in agreement with the fact that the monoclinic (SG 12) structure is the initial phase for this composition. GaTe tubes deserve special attention, since a rectangular morphology is more favorable for them than a hexagonal one in the entire diameter range under consideration. In addition, a comparison of the data in Fig. 4b and d shows that most other NTs formed from the monoclinic phase are energetically more favorable than those formed from hexagonal phases with a diameter of less than 50 Å.

5.2. *Stability of Janus nanotubes generated from MLXY hexagonal layers (M, L = Ga, In; X, Y = S, Te)*

As noted earlier, nanotubes obtained by rolling up of nanolayers with the composition M_2XY (M = Ga, In; X, Y = S, Se, Te; X ≠ Y) are of particular interest, since they can presumably be more stable than binary nanotubes. In this work, the Janus nanotubes of gallium and indium chalcogenides have been modeled for the first time. Here we limited ourselves to Janus NT, which were generated from hexagonal monolayers with LG 69 (*p*3*m*1). These layers can be obtained from the binary layers with LG 78 (*p*–6*m*2) by replacing the chalcogen on one of the two chalcogen surfaces of the monolayer. By design, the considered Janus tubes practically do not differ from similar pristine NT tubes.

However, preliminary calculations confirmed that if a chalcogen atom with a larger effective (van der Waals) radius is located on the outer surface of the tube, and an atom with a smaller radius is located on the inner surface (see Fig. 5), then the mixed tube wins in terms of stability. Only such Janus nanotubes were considered in this study. The optimized parameters of them are given in Table S2 of the SM.

Indeed, the results of ab initio calculations show that the strain energy of Janus monolayers is negative at diameters greater than 30 Å (see Fig. 6a, c). Up to diameters of ≈60 Å, the energy of formation of such Janus tubes relative to bulk parent crystals (see Eq. (5) below) is significantly less than the energy of formation of the corresponding binary systems (see Fig. 6b, d). At the same time, in the region of 50–60 Å, both the strain and formation energies of mixed nanotubes have a minimum. Comparison of plots in Fig. 6b and d also demonstrates that InSTe nanotubes are less stable than GaSTe nanotubes by about 5 kJ mol^{-1}. As in the case of pristine NTs, the armchair and zigzag chiralities have similar energies for the same diameters. Because of this, both chiralities in Figs. 6 (and Fig. 7 below) are combined into common curves.

The formation energy of the Janus nanotubes of the general composition MLXY (M, L = Ga, In; X, Y = S, Te) is estimated relative to the sum of the total energies of two stable parent phases:

$$E_{\text{form}}^{\text{MLXY}}(\text{NT}) = \frac{1}{2}\left(E_{\text{NT}}^{\text{MLXY}}/N_{\text{NT}}^{\text{MLXY}} - E_{\text{bulk}}^{\text{MX}}/N_{\text{bulk}}^{\text{MX}} - E_{\text{bulk}}^{\text{LY}}/N_{\text{bulk}}^{\text{LY}}\right), \quad (5)$$

where $E_{\text{NT}}^{\text{MLXY}}$ and $N_{\text{NT}}^{\text{MLXY}}$ are the energy and number of MLXY formula units in the Janus NT unit cell. Both formation and strain energies are calculated per one metal atom to maintain consistency with results for binary systems. As it was shown above, the replacement of chalcogen in the outer NT shell can significantly improve its stability. In this regard, the question arises, how will the stability of nanotubes change with a similar replacement of a metal atom? To answer this question we have calculated the structure and formation energy of nanotubes obtained by rolling up mixed Ga_2XY monolayers in which the outer Ga atom was replaced by an In atom (see Fig. S1 in SM). In Fig. 7 we compare the strain and formation energies of several ternary NTs with those for one quaternary NT (GaInSTe). Due to the high formation energy of the corresponding monolayer (see Table 3), the strain energy of the GaInSTe nanotube is lower than that of other NTs and is negative, while the formation energy is greater than that of others, except the region of small diameters ($d_{\text{NT}} < 40$ Å). Among the other ternary Janus nanotubes, the Ga_2STe composition exhibits the lowest values of both the strain energy and the formation energy. Thus, we can conclude that the replacement of the Ga atom by the In atom in the penultimate shell on the outer surface of the nanotube does not improve the nanotube stability.

Due to the large size of the nanotubes under consideration (containing from 72 to 400 atoms, see Table S1), we were unable to check the dynamic stability of all of them. Nevertheless, we calculated the phonon frequencies at point Γ of Brillouin zone for a limited number of small-sized pristine and Janus nanotubes with a diameter of 30–40 Å. In addition, using a triple 1D supercell and the extrapolation technique provided in the CRYSTAL17 program [82], we estimated the overall structure of the phonon bands for three selected nanotubes (GaS, GaTe, and Ga_2STe) with chirality (18, 18) and containing 144 atoms each. The obtained results are shown in Figs. S2 and S3 in the Supplementary Material. In all the cases considered, we found no imaginary frequencies. Based on these calculations, it can be assumed that both binary nanotubes and Janus nanotubes considered in this work are dynamically stable.

5.3. *Electronic properties of pristine and Janus nanotubes generated from gallium and indium chalcogenides*

In Fig. 8 we present the diameter dependence of the band gap of binary NT for the different compositions, various parent phases and chirality. Our calculations show that at equal diameters the values of the band gaps of two NT types folded from the layers of the hexagonal (SG 194) and trigonal (SG 166) phases are close and weakly depend on NT chirality. It can be seen (Fig. 8a and b) that calculated diameter dependence for zigzag and armchair binary hexagonal NTs is similar except the region of small diameters. In the zigzag cases (Fig. 8a and c), the E_{gap} monotonically increases with the NT diameter, tending to the relevant monolayer value. The $E_{\text{gap}}(d_{\text{NT}})$ curves are almost parallel and arranged in the same order as for the corresponding monolayers: GaS > GaSe > InS > InSe > GaTe > InTe. Fig. 8d shows that nanotubes generated from the layers of the monoclinic phase have higher values of the band gap, which quickly reaches their limiting value and further does not change.

For the majority of considered pristine nanotubes, the band gap is

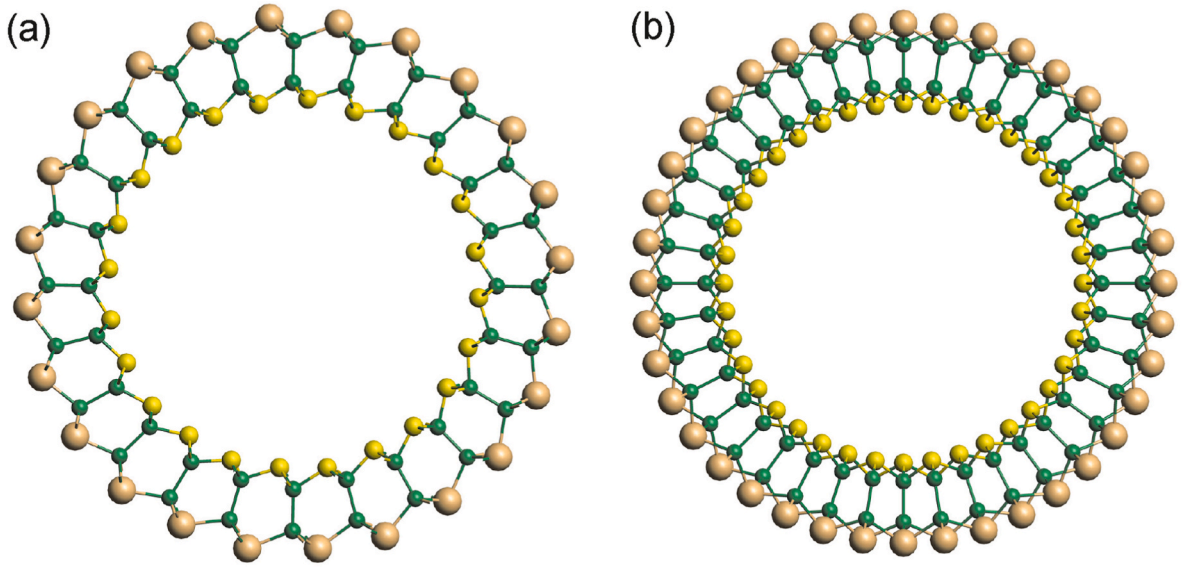

Fig. 5. Optimized structure of Ga_2STe Janus nanotubes. A section perpendicular to the axis of the nanotubes with hexagonal morphology is shown: (a) with armchair chirality (12, 12); (b) with zigzag chirality (20, 0). (Colors in online version: small green spheres are gallium atoms, large beige spheres are tellurium atoms, and middle yellow spheres are sulfur atoms.)

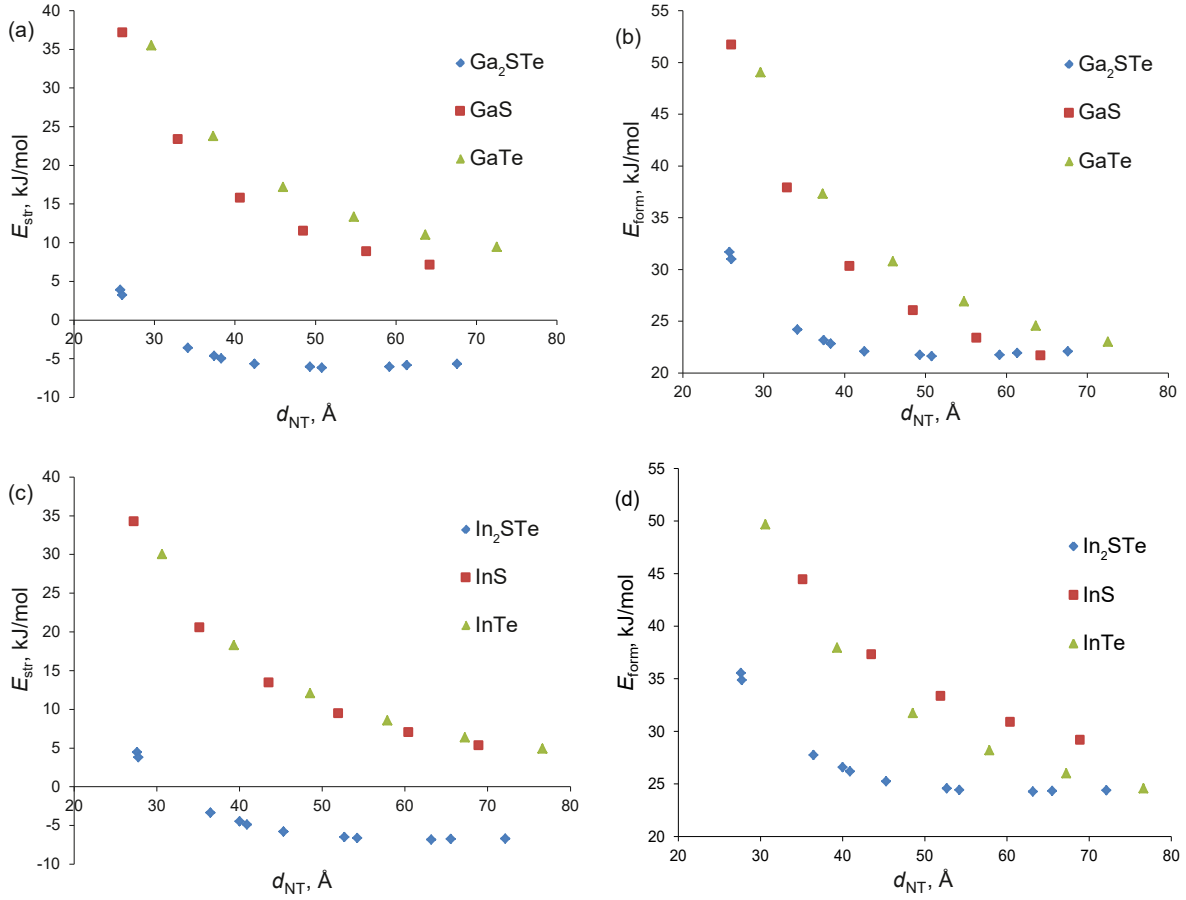

Fig. 6. Strain energies (a, c) and formation energies (b, d) of single-wall pristine and Janus achiral nanotubes obtained by rolling up hexagonal layers of gallium (a, b) and indium (c, d) chalcogenides (data for armchair and zigzag chiralities are shown together).

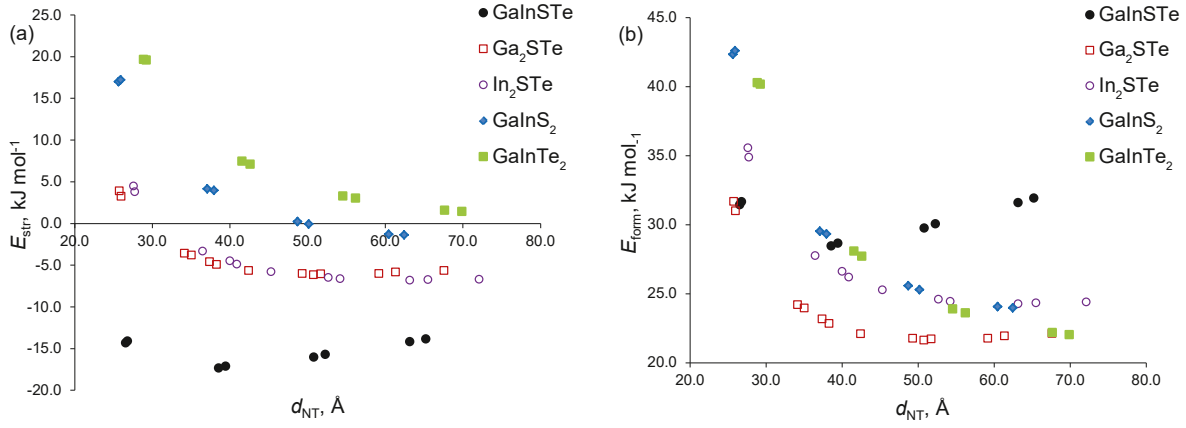

Fig. 7. Strain energies (a) and formation energies (b) of single-wall ternary and quaternary Janus achiral nanotubes obtained by rolling up hexagonal layers of gallium and indium mixed chalcogenides (data for armchair and zigzag chiralities are shown together).

direct. The indirect band gap appears for the armchair chirality of sulfide nanotubes with hexagonal morphology, as well as for the (n, n) chirality of sulfide and selenide nanotubes with rectangular morphology. Nevertheless, at large diameters, most binary SWNTs should have an indirect band gap, since it is observed for monolayers of gallium and indium chalcogenides (see Table 2).

Band gaps obtained for the Janus structures are illustrated in Fig. 9. The NTs which have two different metal atoms, $GaInS_2$ and $GaInTe_2$, reveal the same character of the $E_{gap}(d_{NT})$ dependence as was found for pristine nanotubes. However, the band gap of nanotubes with two different chalcogen atoms shows a non-monotonic dependence on diameter. In this case, the E_{gap} values tend to decrease at the largest of the considered diameters (about 70 Å). The band gap of the ternary Janus nanotubes is mostly direct except the armchair chirality for the $GaInS_2$ nanotube. GaInSTe quaternary nanotubes have a band gap of about 2 eV over the entire considered diameter range. Taking into account that the limiting value of E_{gap} at large diameters should be 1.4 eV (i.e., a monolayer value), we can conclude that GaInSTe nanotubes keep the band gap in the range of 2–1.4 eV at $d_{NT} > 70$ Å. The band gap is direct for all studied GaInSTe nanotubes.

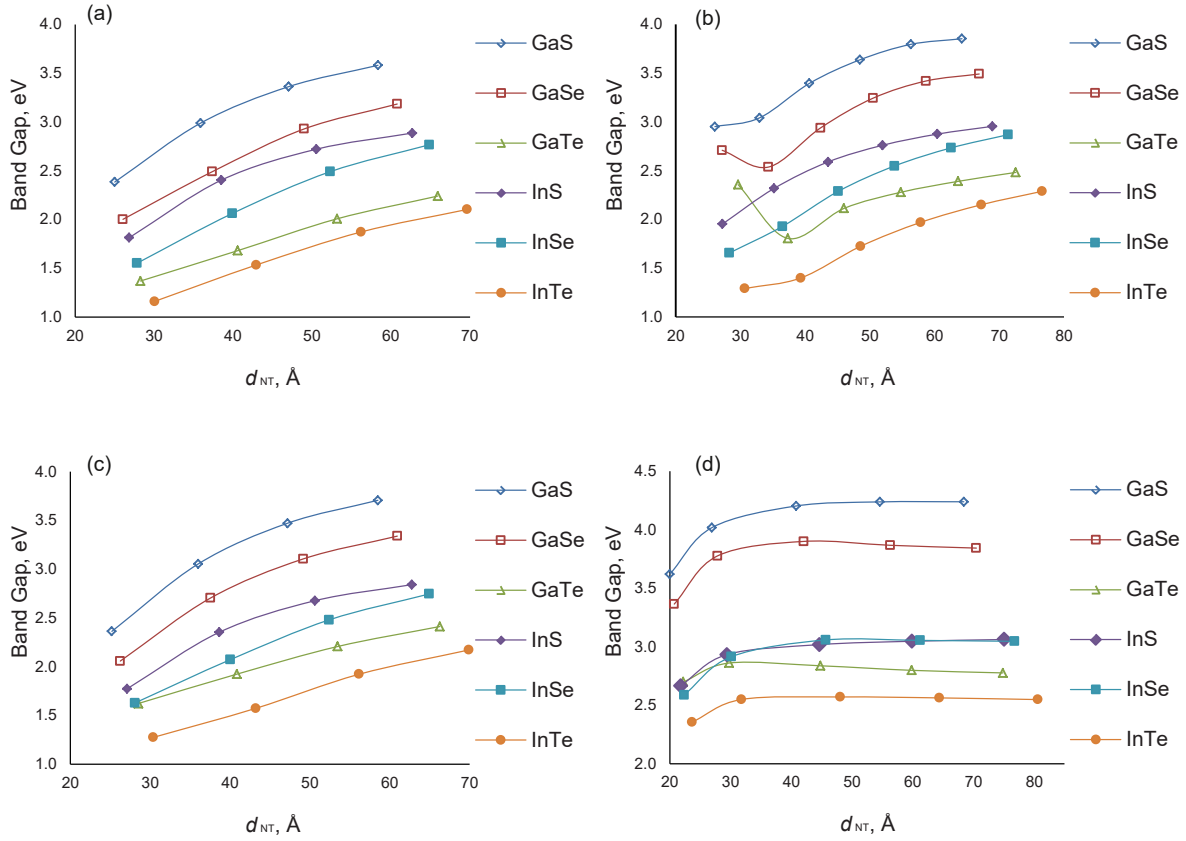

Fig. 8. Diameter dependence of the band gap E_{gap} for binary zigzag (a) and armchair (b) nanotubes folded form the hexagonal layers with LG 78, for zigzag nanotubes folded from the hexagonal layers with LG 72 (c), and for (*n*, *n*) nanotubes of rectangular morphology (d).

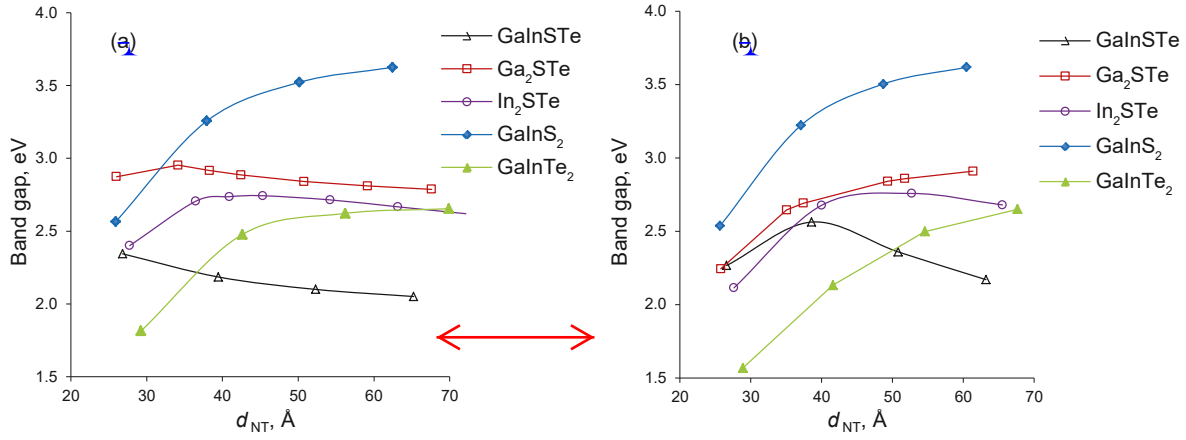

Fig. 9. Diameter dependence of the band gap E_{gap} for Janus zigzag (a) and armchair (b) nanotubes.

On Fig. 10a, we compare the position of the band gaps in binary monolayers and nanotubes calculated in this work. The water oxidation O_2/H_2O (−5.67 eV) and hydrogen reduction H^+/H_2 (−4.44 eV) potentials relative to the vacuum level at zero pH are shown as the straight lines. It is easy to see that our results for MX monolayers (M = Ga, In, X = S, Te) are in fairly good agreement with the results of Zhuang and Hennig [2] obtained using the quasiparticle approximation of many-body perturbation theory. The relative arrangement of the band edges for the selected nanotubes resembles that for the corresponding monolayers. However, the band gaps in nanotubes are narrower that E_{gap} in monolayers due to the simultaneous increase in the valence band maximum (VBM) and decrease in the conduction band minimum (CBM). Our data are consistent with the conclusion [2] that MX nanosystems are suitable photocatalysts for water splitting. Due to the reduction in the band gap, MX nanotubes allow more light to be absorbed in the visible range than MX monolayers. Based on the data obtained, it can be assumed that the composition GaTe or InTe is the most suitable for photocatalysis using the binary nanotubes. By varying the diameter or the number of NT walls, the band gap can be adjusted to 1.75–2.5 eV, which corresponds to the center of the visible light region.

Fig. 10b demonstrates the band edges calculated for Janus monolayers and nanotubes. It can be assumed [35] that the transition from binary systems to Janus systems will allow finer tuning of the properties of photocatalysts by selecting specific Janus structures. Our data for

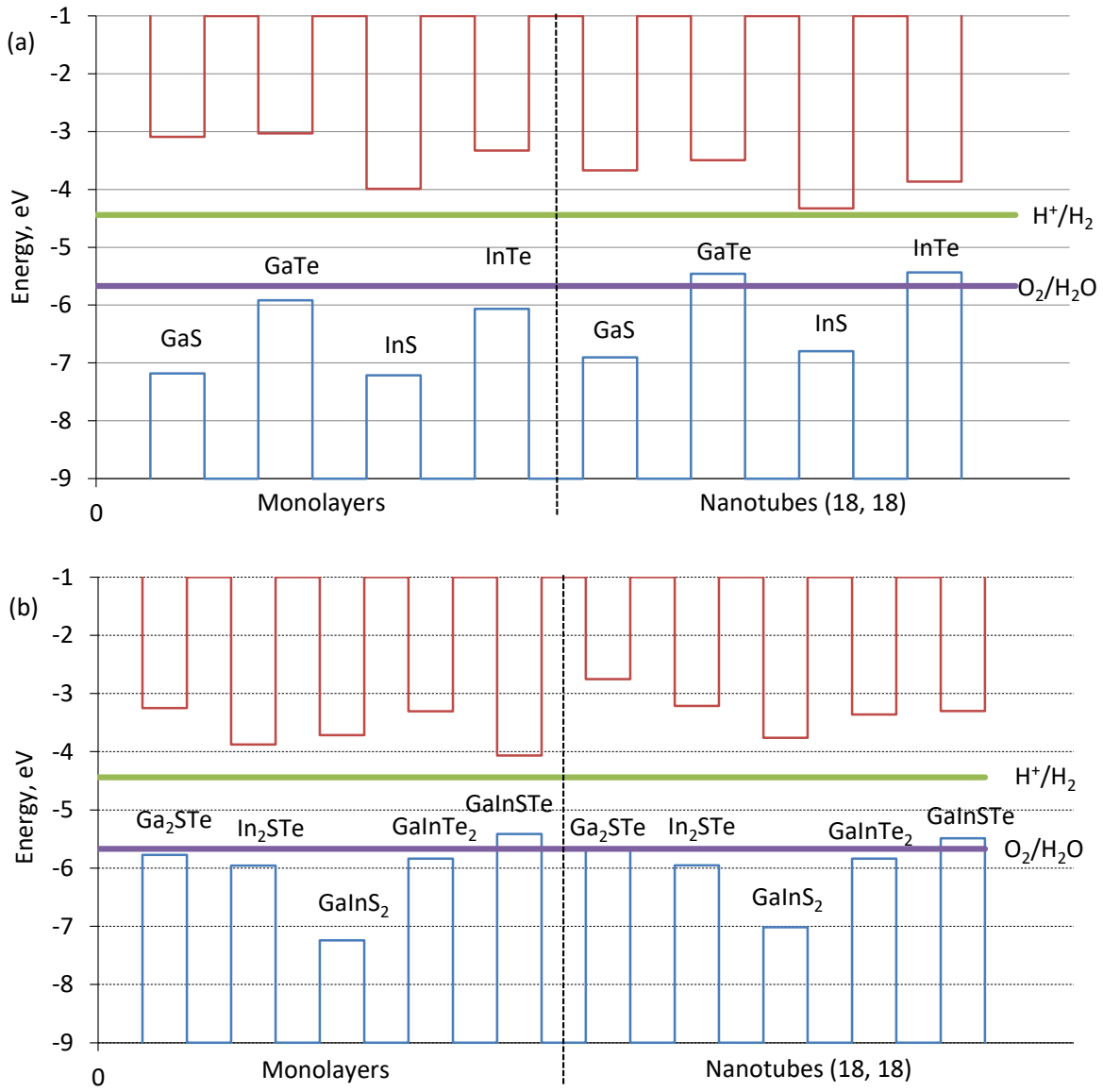

Fig. 10. Edge positions of the valence and conduction bands in the selected pristine (a) and Janus (b) monolayers and nanotubes.

Ga_2STe and In_2STe monolayers qualitatively agree with those reported by Bai et al. [35], but our band gaps somewhat wider. By this reason our computations show that VBM of the Janus Ga_2STe monolayer, as well as that of In_2STe monolayer, are not higher than the water oxidation potential of O_2/H_2O. Thus, from our point of view, both systems are suitable for water splitting in the visible light region (with band gaps of 2.5 eV and 2.1 eV, respectively, see Table 3).

It is interesting to note, and this, presumably, was discovered for the first time, that in the case of ternary systems M_2XY or MLXY ($X \neq Y$), the band gap of nanotubes may be slightly larger than the band gap of the parent monolayers (in contrast to binary monochalcogenides) due to an increase of the CBM in nanotubes. As a result, it can be assumed that all the compositions considered for Janus nanotubes, except for $GaInS_2$ ($E_{gap} > 3$ eV), are potentially capable of exhibiting photocatalytic activity in the visible region. Our data on Janus nanotubes confirm the conclusion made for Janus monolayers [35,36] that the presence of Te is desirable for good photocatalytic ability.

To study the influence of deformation on the electronic properties of pristine and Janus NTs, we have calculated the band gap of gallium chalcogenides at different axial strains (see Fig. 11). We found that the band gap E_{gap} of nanotubes depends non-monotonically on the strain ε caused by the applied stress. The band gap for all considered types of tubes decreases both under compression and stretching (see Fig. 11), and the maximum is observed either at the equilibrium period of the nanotube, or it is somewhat shifted towards negative or positive strains. The dependence of the band gap for the Janus NTs has a form of two straight lines intersecting in the region of small positive strains with $\varepsilon \approx 0.05$. It should be noted that the nanotubes under consideration are capable of withstanding significant stretching: they retain their structure and integrity up to an elongation of 25%. In the entire region of examined deformations, the following relation takes place: $E_{gap}(Ga_2STe) \geq E_{gap}(GaTe)$. At equilibrium UC periods $E_{gap}(Ga_2STe) \approx E_{gap}(GaS)$, but at negative and positive strains, the band gap of Ga_2STe nanotubes can be either smaller or slightly larger than the value for gallium sulfide. The found strong dependence of the E_{gap} on stress makes it possible to use this effect to tune the band gap of the systems under consideration towards smaller values.

Our calculations also indicated that the effect of small torsional stresses (see next section) is different for nanotubes of different chirality. The band gap of armchair nanotubes decreases with twisting, while the

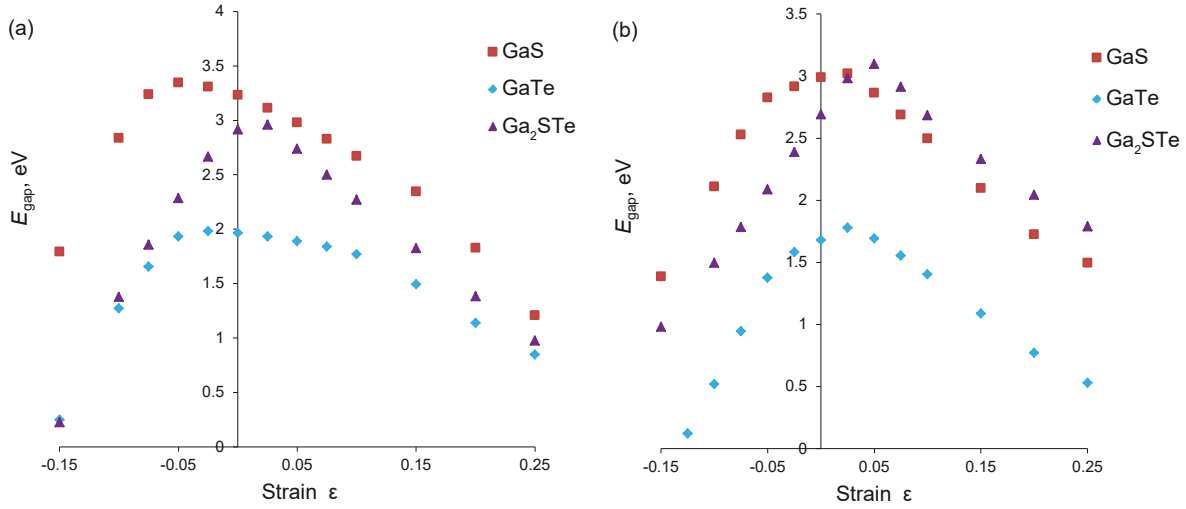

Fig. 11. Dependence of the band gap in GaS, GaTe, and Ga_2STe nanotubes with (a) (18, 18) and (b) (30, 0) chiralities on the strain caused by stress along the tube axis.

band gap of zigzag nanotubes turned out to be insensitive to twisting, at least at small torsion angles.

5.4. Elastic properties of pristine and Janus nanotubes generated from gallium chalcogenides

The computation of the elastic properties of nanotubes based on gallium sulfide and telluride has been performed for the first time. We have calculated the Young's modulus (Y), shear modulus (G) and Poisson's ratio (ν).

The second derivative of the total energy E with respect to the axial strain $\varepsilon_{\|}$ has been used to calculate the Young's modulus of nanotubes [83]:

$$Y = \frac{1}{V_0} \times \frac{\partial^2 E}{\partial \varepsilon_{\|}{}^2}. \tag{6}$$

The equilibrium volume V_0 of the nanotube translational unit can be determined as follows:

$$V_0 = 2\pi\, R_0\, L_0\, W_0, \tag{7}$$

where R_0 indicates the average radius of the unstressed nanotube, and L_0 and W_0 are the corresponding length and thickness. In general case, the parameters R and W can be defined using some model assumptions [59]. In the case of Ga_2XY nanotubes (X, Y = S, Te), we can write:

$$R = (R_{\max} + R_{\min} + |r_X - r_Y|) / 2, \tag{8}$$

$$W = R_{\max} - R_{\min} + r_X + r_Y, \tag{9}$$

where r_S and r_{Te} are the effective atomic radii of S and Te, evaluated from the interlayer distances in bulk chalcogenides. The values estimated by us are $r_S = 1.529$ Å, $r_{Te} = 1.813$ Å [59].

The Poisson's ratio can be determined as a ratio of transverse NT contraction to axial NT elongation:

$$\nu = -\frac{L_0}{R_0} \times \frac{\partial R}{\partial L}. \tag{10}$$

To calculate shear modulus we used the following equation [83]:

$$G = \frac{1}{V_0} \times \frac{\partial^2 E}{\partial \gamma^2}; \quad \gamma = \frac{\varphi R}{L}, \tag{11}$$

where φ is the torsion angle. In the case of a transversely isotropic system, the values of Y, G and ν should obey the relation:

$$G = \frac{Y}{2(1+\nu)}, \tag{12}$$

which can also be used to roughly estimate the shear modulus of nanotubes.

Using Eqs. (6) and (10) we have estimated Young's modulus and Poisson's ratio for GaS, GaTe and Ga_2STe nanotubes with several chiralities (see Table S3). To obtain the energy second derivatives in Eq. (6), the dependences of the total energy on the axial strain were calculated. Fig. 12 shows the energy vs. strain for two chiralities (18, 18) and (30, 0), which have close diameters for a given composition. It is interesting to note that the curves presented in Fig. 12 show very little variance between the considered compounds. The inequalities between the obtained values of Young's moduli (see below) are due exclusively to variations in the equilibrium volume V_0 of the nanotube translational unit.

The shear modulus has been explicitly determined (Eq. (11)) for the same two chiralities (18, 18) and (30, 0). The adopted procedure is based on the line group theory [79]. For both considered chiralities, we constructed the twisted nanotubes with a sufficiently small torsional angle (≈0.5°) and acceptable translational periods. The methodology used is given in more details in our recent work [84], where it was applied for nanohelicenes.

The obtained results are given in Table 4 (More complete data on Young's modulus and Poisson's ratio are presented in Table S3 of the SM).

The data in Table 4 indicate a gradual decrease in both moduli and Poisson's ratio in the series GaS > Ga_2STe > GaTe. For Young's moduli a weak dependence on chirality and diameter was found (see Table S3 in SM). For diameters in the range of 30–60 Å, the values of Y lie in the intervals: 103–108 GPa for GaS; 85–88 GPa for Ga_2STe; and 70–72 GPa for GaTe NTs. Poisson's ratio depends on diameter and chirality to a much greater extent than Young's modulus. Thus, the values of ν for armchair nanotubes are higher than for zigzag nanotubes in accordance with the results of Lorenz et al. [83] for MoS_2 nanotubes. The same is true for the shear modulus calculated directly from Eq. (11). However, the shear modulus calculated from Eq. (12) exhibits a week dependence on chirality, which should be due to the approximate nature of this relation. Ultimately, it can be concluded that armchair-type nanotubes are more rigid with respect to twisting compared to zigzag-type nanotubes. In general, however, nanotubes based on gallium chalcogenides seem to have lower rigidity than nanotubes based on molybdenum dichalcogenides. Indeed, the calculated values of the elastic moduli of

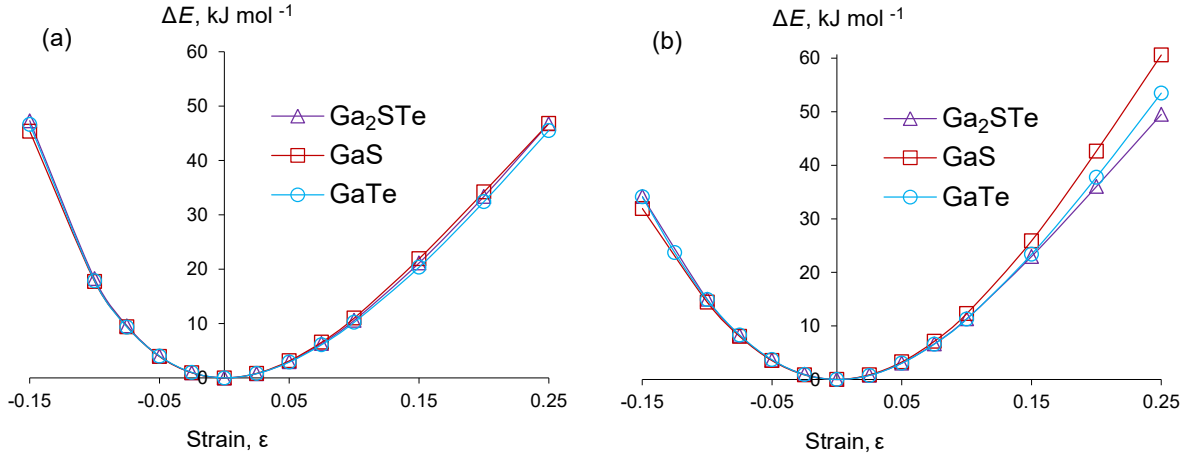

Fig. 12. Dependence of the total energy on axial strain in GaS, GaTe, and Ga_2STe nanotubes with (a) (18, 18) and (b) (30, 0) chiralities.

Table 4
Elastic properties of pristine and Janus GaXY nanotubes (X, Y = S, Te) generated from the monolayers of hexagonal phases (SG 194) with chiralities (18, 18) and (30, 0).

Crystal	Period, a (Å)	Average radius, R (Å)	Thickness, W (Å)	Poisson's ratio, ν	Young's modulus, Y (GPa)	Shear modulus	
						G^a (GPa)	G^b (GPa)
(18, 18)							
GaS	3.63	18.38	7.68	0.317	105.7	40.1	48.3
Ga_2STe	3.88	19.29	8.19	0.280	85.8	33.5	40.0
GaTe	4.10	20.81	8.60	0.275	69.4	27.2	34.0
(30, 0)							
GaS	6.21	17.94	7.67	0.270	102.8	40.5	36.8
Ga_2STe	6.62	18.84	8.19	0.245	84.6	34.0	32.0
GaTe	7.01	20.29	8.60	0.226	69.1	28.2	25.4

[a] Shear modulus estimated from approximate Eq. (12).
[b] Shear modulus calculated from Eq. (11).

gallium monosulfide NTs are approximately two times lower than those for molybdenum disulfide NTs [83,85].

6. Conclusions

In this work, we simulated a large set of single-wall nanotubes rolled up from monolayers cut from various bulk phases of indium and gallium chalcogenides. The stability of the considered nanotubes with respect to both bulk phases (E_{form}) and single monolayers (E_{str}) is estimated. We suppose that the formation energies relative to the most stable bulk phases provide a more correct comparison between nanotubes of different composition. We found that the stability of NTs folded from the layers of two hexagonal polymorphs with symmetries p–6m2 and p–3m1 practically do not differ. Moreover, the strain E_{str} and formation E_{form} energies of the armchair and zigzag NTs with hexagonal morphology are very close at equal diameters. At a given NT diameter, the formation energies of Ga chalcogenides are lower than the formation energies of In chalcogenides. In general, the E_{form} of nanotubes with hexagonal morphology increases in the following order: GaS < GaSe ≈ GaTe < InSe < InTe < InS. On the other hand, GaTe NTs with a rectangular morphology turned out to be the most stable due to the fact that the parent monoclinic (SG 12) phase is the ground state for the GaTe bulk. A comparison of the two morphologies shows that most NTs generated from the monoclinic phase are energetically more favorable than NTs formed from hexagonal phases if their diameter is less than 50 Å. GaTe tubes of rectangular morphology have an energy advantage over hexagonal tubes in the entire range of diameters studied.

Our calculations support the assumption that Janus nanotubes have the lower formation energy than their pristine counterparts if the heavier chalcogen atom is located on the outer surface of the nanotube. In addition, it was established that the diameter dependences of the strain and formation energy of Janus nanotubes have a minimum between 50 and 60 Å. Among ternary Janus nanotubes, Ga_2STe nanotubes have the lowest values of both strain and formation energies. Replacing the Ga atom with an In atom in the penultimate outer shell does not improve the nanotube stability. Preliminary calculations of phonon frequencies testify to the dynamical stability of both pristine and Janus nanotubes.

The electron band gap is direct for the majority of considered binary nanotubes. The indirect band gap appears for the armchair chirality of sulfide nanotubes with hexagonal morphology, as well as for sulfide and selenide nanotubes with rectangular morphology. The values of the SWNT band gap is decreased in the following sequence: GaS > GaSe > InS > InSe > GaTe > InTe, and increased with NT diameter. However, the band gap of Janus nanotubes with two different chalcogen atoms shows a non-monotonic dependence on diameter. In this case, the E_{gap} values tend to decrease at the largest of the considered diameters (about 70 Å).

Our computations confirm that Janus monolayers and nanotubes can potentially be useful for photocatalytic applications, exhibiting adsorption in the visible light region. The presence of Te atoms is desirable for good photocatalytic performance of both Janus monolayers and nanotubes.

The band gap for all considered types of tubes decreases both under compression and under tension. The maximum value of E_{gap} is observed near the equilibrium 1D translational period of the nanotube. The band gap of armchair nanotubes also decreases upon twisting, while the band gap of zigzag nanotubes is insensitive to twisting, at least at small twist angles.

The calculations of the elastic moduli of pristine and Janus

nanotubes generated from gallium sulfides and tellurides indicate that they have lower rigidity than nanotubes based on molybdenum dichalcogenides. The data obtained for Young's modulus demonstrate a weak dependence on both the chirality type and diameter. However, the shear moduli, as well as the Poisson's ratios of armchair nanotubes are higher than those for zigzag nanotubes of equal diameter. The Poisson's ratio also decreases with the nanotube diameter. All mentioned elastic moduli decrease in the sequence: GaS > Ga_2STe > GaTe.

Declaration of competing interest

The authors declare that they have no known competing financial interests or personal relationships that could have appeared to influence the work reported in this paper.

Data availability

Data will be made available on request.

Acknowledgements

The reported study was funded by the Russian Foundation for Basic Research within the framework of research project no. 20-03-00271 and accomplished using the computational facilities of the Resource Center "Computer Center of St. Petersburg State University".

Appendix A. Supplementary data

Supplementary data to this article can be found online at https://doi.org/10.1016/j.physe.2022.115611.

References

[1] W. Huang, L. Gan, H. Li, Y. Ma, T. Zhai, 2D layered group IIIA metal chalcogenides: synthesis, properties and applications in electronics and optoelectronics, CrystEngComm 18 (2016) 3968–3984, https://doi.org/10.1039/c5ce01986a.
[2] H.L. Zhuang, R.G. Hennig, Single-layer group-III monochalcogenide photocatalysts for water splitting, Chem. Mater. 25 (2013) 3232–3238, https://doi.org/10.1021/cm401661x.
[3] K.R. Allakhverdiev, M.Ö. Yetis, S. Özbek, T.K. Baykara, E. Yu Salaev, Effective nonlinear GaSe crystal. Optical properties and applications, Laser Phys. 19 (2009) 1092–1104, https://doi.org/10.1134/S1054660X09050375.
[4] Z.A. Jahangirli, F.M. Gashizade, D.A. Guseinova, B.G. Mekhtiev, N.B. Mustafaev, First-principles calculation of the photothreshold of a β-GaS layered crystal, Phys. Solid State 58 (2016) 1764–1766, https://doi.org/10.1134/S1063783416090134.
[5] S.S.A. Al-Abbas, M.K. Muhsin, H.R. Jappor, Tunable optical and electronic properties of gallium telluride monolayer for photovoltaic absorbers and ultraviolet detectors, Chem. Phys. Lett. 713 (2018) 46–51, https://doi.org/10.1016/j.cplett.2018.10.020.
[6] V. Zólyomi, N.D. Drummond, V.I. Fal'ko, Electrons and phonons in single layers of hexagonal indium chalcogenides from ab initio calculations, Phys. Rev. B 89 (2014), 205416, https://doi.org/10.1103/PhysRevB.89.205416.
[7] J. Jalilian, M. Safari, Electronic and optical properties of α-InX (X =S, Se and Te) monolayer: under strain conditions, Phys. Lett. 381 (2017) 1313–1320, https://doi.org/10.1016/j.physleta.2017.01.024.
[8] D.M. Hoat, Comparative study of structural electronic optical and thermoelectric properties of GaS bulk and monolayer, Philos. Mag. A 99 (2019) 736–751, https://doi.org/10.1080/14786435.2018.1560513.
[9] A.V. Bandura, A.V. Kovalenko, D.D. Kuruch, R.A. Evarestov, Lattice dynamics and thermodynamic properties of bulk phases and monolayers of GaTe and InTe: a comparison from first-principles calculations, Eur. J. Inorg. Chem. 2021 (2021) 126–138, https://doi.org/10.1002/ejic.202000634.
[10] S.J. Magorrian, V. Zólyomi, N.D. Drummond, Structures of bulk hexagonal post transition metal chalcogenides from dispersion-corrected density functional theory, Phys. Rev. B 103 (2021), 094118, https://doi.org/10.1103/PhysRevB.103.094118.
[11] Q. Liu, J.-J. Li, D. Wu, X.-Q. Deng, Z.-H. Zhang, Z.-Q. Fan, K.-Q. Chen, Gate-controlled reversible rectifying behavior investigated in a two-dimensional MoS2 diode, Phys. Rev. B 104 (2021), 045412, https://doi.org/10.1103/PhysRevB.104.045412.
[12] Z.-Q. Fan, Z.-H. Zhang, S.-Y. Yang, High-performance 5.1 nm in-plane Janus WSeTe Schottky barrier field effect transistors, Nanoscale 12 (2020) 21750–21756, https://doi.org/10.1039/d0nr05269h.
[13] X. Zhou, J. Cheng, Y. Zhou, T. Cao, H. Hong, Z. Liao, S. Wu, H. Peng, K. Liu, D. Yu, Strong second-harmonic generation in atomic layered GaSe, J. Am. Chem. Soc. 137 (2015) 7994–7997, https://doi.org/10.1021/jacs.5b04305.
[14] S. Das, C. Ghosh, O.G. Voevodina, YuM. Andreev, S.Yu Sarkisov, Modified GaSe crystal as a parametric frequency converter, Appl. Phys. B 82 (2006) 43–46, https://doi.org/10.1007/s00340-005-2024-x.
[15] P. Reshmi, A. Kunjomana, K. Chandrasekharan, M. Meena, C. Mahadevan, Structural, electrical and mechanical properties of GaTe for radiation detector applications, Int. J. Soft Comput. Eng. 1 (2011) 228–232. https://www.ijsce.org/wp-content/uploads/papers/v1i5/E0202101511.pdf.
[16] J. Martínez-Pastor, A. Segura, J.L. Valdés, A. Chevy, Electrical and photovoltaic properties of indium-tin-oxide/p-InSe/Au solar cells, J. Appl. Phys. 62 (1987) 1477–1483, https://doi.org/10.1063/1.339627.
[17] Y. Wang, K. Szökölová, M.Z.M. Nasir, Z. Sofer, M. Pumera, Electrochemistry of layered semiconducting $A^{III}B^{VI}$ chalcogenides: indium monochalcogenides (InS, InSe, InTe), ChemCatChem 11 (2019) 2634–2642, https://doi.org/10.1002/cctc.201900449.
[18] X. Wang, Y. Sheng, R.-J. Chang, J.K. Lee, Y. Zhou, S. Li, T. Chen, H. Huang, B. F. Porter, H. Bhaskaran, J.H. Warner, Chemical vapor deposition growth of two-dimensional monolayer gallium sulfide crystals using hydrogen reduction of Ga_2S_3, ACS Omega 3 (2018) 7897–7903, https://doi.org/10.1021/acsomega.8b00749.
[19] Z. Wang, M. Safdar, M. Mirza, K. Xu, Q. Wang, Y. Huang, F. Wang, X. Zhan, J. He, High-performance flexible photodetectors based on GaTe nanosheets, Nanoscale 7 (2015) 7252–7258, https://doi.org/10.1039/c4nr07313d.
[20] X. Li, J. Dong, J.C. Idrobo, A.A. Puretzky, C.M. Rouleau, D.B. Geohegan, F. Ding, K. Xiao, Edge-controlled growth and etching of two-dimensional GaSe monolayers, J. Am. Chem. Soc. 139 (2017) 482–491, https://doi.org/10.1021/jacs.6b11076.
[21] F. Li, M. Chen, Y. Wang, X. Zhu, X. Zhang, Z. Zou, D. Zhang, J. Yi, Z. Li, D. Li, A. Pan, Strain-controlled synthesis of ultrathin hexagonal GaTe/MoS_2 heterostructure for sensitive photodetection, iScience 24 (2021), 103031, https://doi.org/10.1016/j.isci.2021.103031.
[22] J. Zhou, J. Shi, Q. Zeng, Y. Chen, L. Niu, F. Liu, T. Yu, K. Suenaga, X. Liu, J. Lin, Z. Liu, InSe monolayer: synthesis, structure and ultra-high second-harmonic generation, 2D Mater. 5 (2018), 025019, https://doi.org/10.1088/2053-1583/aab390.
[23] P. Marvan, V. Mazánek, Z. Sofer, Shear-force exfoliation of indium and gallium chalcogenides for selective gas sensing applications, Nanoscale 11 (2019) 4310–4317, https://doi.org/10.1039/c8nr09294j.
[24] P.A. Hu, L.F. Wang, M. Yoon, J. Zhang, W. Feng, X.N. Wang, Z.Z. Wen, J.C. Idrobo, Y. Miyamoto, D.B. Geohegan, K. Xiao, Highly responsive ultrathin GaS nanosheet photodetectors on rigid and flexible substrates, Nano Lett. 13 (2013) 1649–1654, https://doi.org/10.1021/nl400107k.
[25] Y. Wang, Y. Zhao, X. Ding, L. Qiao, Recent advances in the electrochemistry of layered post-transition metal chalcogenide nanomaterials for hydrogen evolution reaction, J. Energy Chem. 60 (2021) 451–479, https://doi.org/10.1016/j.jechem.2021.01.021.
[26] M. Yagmurcukardes, Y. Qin, S. Ozen, M. Sayyad, F.M. Peeters, S. Tongay, H. Sahin, Quantum properties and applications of 2D Janus crystals and their superlattices, Appl. Phys. Rev. 7 (2020), 011311, https://doi.org/10.1063/1.5135306.
[27] Y.C. Lin, C. Liu, Y. Yu, E. Zarkadoula, M. Yoon, A.A. Puretzky, L. Liang, X. Kong, Y. Gu, A. Strasser, H.M. Meyer III, M. Lorenz, M.F. Chisholm, I.N. Ivanov, C. M. Rouleau, G. Duscher, K. Xiao, D.B. Geohegan, Low energy implantation into transition-metal dichalcogenide monolayers to form Janus structures, ACS Nano 14 (2020) 3896–3906, https://doi.org/10.1021/acsnano.9b10196.
[28] A.Y. Lu, H. Zhu, J. Xiao, C.P. Chuu, Y. Han, M.H. Chiu, C.C. Cheng, C.W. Yang, K. H. Wei, Y. Yang, Y. Wang, D. Sokaras, D. Nordlund, P. Yang, D.A. Muller, M. Y. Chou, X. Zhang, L.J. Li, Janus monolayers of transition metal dichalcogenides, Nat. Nanotechnol. 12 (2017) 744–749, https://doi.org/10.1038/nnano.2017.100.
[29] J. Zhang, S. Jia, I. Kholmanov, L. Dong, D. Er, W. Chen, H. Guo, Z. Jin, V.B. Shenoy, L. Shi, J. Lou, Janus monolayer transition-metal dichalcogenides, ACS Nano 11 (2017) 8192–8198, https://doi.org/10.1021/acsnano.7b03186.
[30] Y. Guo, S. Zhou, Y. Bai, J. Zhao, Enhanced piezoelectric effect in Janus group-III chalcogenide monolayers, Appl. Phys. Lett. 110 (2017), 163102, https://doi.org/10.1063/1.4981877.
[31] A. Kandemir, H. Sahin, Janus single layers of In_2SSe: a first-principles study, Phys. Rev. B 97 (2018), 155410, https://doi.org/10.1103/PhysRevB.97.155410.
[32] A. Betal, J. Sera, M. Alam, A.N. Gandi, S. Sahu, Strain and electric field-modulated indirect-to-direct band transition of monolayer $GaInS_2$, J. Comput. Electron. 21 (2022) 227–234, https://doi.org/10.1007/s10825-021-01833-1.
[33] H.D. Bui, H.R. Jappor, N.N. Hieu, Tunable optical and electronic properties of Janus monolayers Ga_2SSe, Ga_2STe, and Ga_2SeTe as promising candidates for ultraviolet photodetectors applications, Superlattice. Microst. 125 (2019) 1–7, https://doi.org/10.1016/j.spmi.2018.10.020.
[34] K.J. Pang, Y.D. Wei, W.Q. Li, X. Zhou, Y.J. Jiang, J.Q. Yang, X.J. Li, L. Gao, Y. Y. Jiang, Highly sensitive gas sensing material for polar gas molecule based on Janus group-III chalcogenide monolayers: a first-principles investigation, Sci. China Technol. Sci. 63 (2020) 1566–1576, https://doi.org/10.1007/s11431-020-1616-9.
[35] Y. Bai, Q. Zhang, N. Xu, K. Deng, E. Kan, The Janus structures of group-III chalcogenide monolayers as promising photocatalysts for water splitting, Appl. Surf. Sci. 478 (2019) 522–531, https://doi.org/10.1016/j.apsusc.2019.02.004.
[36] A. Huang, W. Shi, Z. Wang, Optical properties and photocatalytic applications of two-dimensional Janus group-III monochalcogenides, J. Phys. Chem. C 123 (2019) 11388–11396, https://doi.org/10.1021/acs.jpcc.8b12450.
[37] T. Wang, F. Chi, M. Chen, J. Liu, Giant photogalvanic effect in Janus monolayer In_2SSe, Opt Commun. 492 (2021), 126945, https://doi.org/10.1016/j.optcom.2021.126945.
[38] H. Zhao, Y. Gu, N. Lu, Y. Liu, Y. Ding, B. Ye, X. Huo, B. Bian, C. Wei, X. Zhang, G. Yang, Janus In_2SeTe for photovoltaic device applications from first-principles

study, Chem. Phys. 553 (2022), 111384, https://doi.org/10.1016/j.chemphys.2021.111384.
[39] P.A. Hu, Y.Q. Liu, L. Fu, L.C. Cao, D.B. Zhu, GaS multi-walled nanotubes from the lamellar precursor, Appl. Phys. A 80 (2005) 1413–1417, https://doi.org/10.1007/s00339-004-3187-8.
[40] U.K. Gautam, S.R.C. Vivekchand, A. Govindaraj, G.U. Kulkarni, N.R. Selvi, C.N. R. Rao, Generation of Onions and Nanotubes of GaS and GaSe through Laser and Thermally Induced Exfoliation, J. Am. Chem. Soc. 127 (2005) 3658–3659, https://doi.org/10.1021/ja042294k.
[41] A. Seral-Ascaso, S. Metel, A. Pokle, C. Backes, C.J. Zhang, H.C. Nerl, K. Rode, N. C. Berner, C. Downing, N. McEvoy, E. Muñoz, A. Harvey, Z. Gholamvand, G. S. Duesberg, J.N. Coleman, V. Nicolosi, Long-chain amine-templated synthesis of gallium sulfide and gallium selenide nanotubes, Nanoscale 8 (2016) 11698–11706, https://doi.org/10.1039/c6nr01663d.
[42] X. Meng, K. He, D. Su, X. Zhang, C. Sun, Y. Ren, H.-H. Wang, W. Weng, L. Trahey, C.P. Canlas, J.W. Elam, Gallium sulfide–single-walled carbon nanotube composites: high-performance anodes for lithium-ion batteries, Adv. Funct. Mater. 24 (2014) 5435–5442, https://doi.org/10.1002/adfm.201401002.
[43] Y.H. Kim, J.H. Lee, D.-W. Shin, S.M. Park, J.S. Moon, J.G. Nam, J.-B. Yoo, Synthesis of shape-controlled β-In_2S_3 nanotubes through oriented attachment of nanoparticles, Chem. Commun. 46 (2010) 2292–2294, https://doi.org/10.1039/b922366e.
[44] G. Liu, X. Jiao, Z. Qin, D. Chen, Solvothermal preparation and visible photocatalytic activity of polycrystalline β-In_2S_3 nanotubes, CrystEngComm 13 (2011) 182–187, https://doi.org/10.1039/c0ce00084a.
[45] T. Köhler, T. Frauenheim, Z. Hajnal, G. Seifert, Tubular structures of GaS, Phys. Rev. B 69 (2004), 193403, https://doi.org/10.1103/PhysRevB.69.193403.
[46] A.N. Enyashin, O. Brontvein, G. Seifert, R. Tenne, Structure and stability of GaS fullerenes and nanotubes, Isr. J. Chem. 57 (2017) 529–539, https://doi.org/10.1002/ijch.201600121.
[47] D. Porezag, T. Frauenheim, T. Köhler, G. Seifert, R. Kaschner, Construction of tight-binding-like potentials on the basis of density-functional theory: application to carbon, Phys. Rev. B 51 (1995) 12947–12957, https://doi.org/10.1103/PhysRevB.51.12947.
[48] M. Côté, M.L. Cohen, D.J. Chadi, Theoretical study of the structural and electronic properties of GaSe nanotubes, Phys. Rev. B 58 (1998) R4277. –R4280, https://proxy.library.spbu.ru:2060/10.1103/PhysRevB.58.R4277.
[49] V.V. Karpov, A.V. Bandura, R.A. Evarestov, Nonempirical calculations of the structure and stability of nanotubes based on gallium monochalcogenides, Phys. Solid State 62 (2020) 1017–1023, https://doi.org/10.1134/S1063783420060116.
[50] A.V. Bandura, D.D. Kuruch, R.A. Evarestov, First-principles calculations of InS-based nanotubes, Isr. J. Chem. 56 (2016) 490–500, https://doi.org/10.1002/ijch.201600054.
[51] N. Yoshinaga, S. Aomine, Imogolite in some ando soils, Soil Sci. Plant Nutr. 8 (1962) 22–29, https://doi.org/10.1080/00380768.1962.10430993.
[52] T.F. Bates, F.A. Hildebrand, A. Swineford, Morphology and structure of endellite and halloysite, Am. Mineral.: Journal of Earth and Planetary Materials 35 (1950) 463–484.
[53] E. Whittaker, The structure of chrysotile. II. Clino-chrysotile, Acta Crystallogr. 9 (1956) 855–862, https://doi.org/10.1107/S0365110X5600245X.
[54] V. Farmer, A. Fraser, J. Tait, Synthesis of imogolite: a tubular aluminium silicate polymer, J. Chem. Soc., Chem. Commun. 13 (1977) 462–463, https://doi.org/10.1039/C39770000462.
[55] C. Li, J. Wanga, X. Luo, S. Ding, Large scale synthesis of Janus nanotubes and derivative nanosheets by selective etching, J. Colloid Interface Sci. 420 (2014) 1–8, https://doi.org/10.1016/j.jcis.2013.12.062.
[56] R.A. Evarestov, A.V. Kovalenko, A.V. Bandura, Janus MoSSe Nanotubes: first-Principles study on stability, structural and electronic properties of monolayers and nanotubes based on pure Mo(W)S(Se)2 and mixed (Janus) Mo(W)SSe dichalcogenides, Physica E 115 (2020), 113681, https://doi.org/10.1016/j.physe.2019.113681.
[57] W.-J. Yin, H.-J. Tan, P.-J. Ding, B. Wen, X.-B. Li, G. Teobaldi, L.-M. Liu, Recent advances in low-dimensional Janus materials: theoretical and simulation perspectives, Mater. Adv. 2 (2021) 7543–7558, https://doi.org/10.1039/d1ma00660f.
[58] F.T. Bölle, A.E.G. Mikkelsen, K.S. Thygesen, T. Vegge, I.E. Castelli, Structural and chemical mechanisms governing stability of inorganic Janus nanotubes, npj Comput, Mater 7 (2021) 41, https://doi.org/10.1038/s41524-021-00505-9.
[59] S.I. Lukyanov, A.V. Bandura, R.A. Evarestov, Structure and stability of GaS, GaTe, and Janus-Ga_2STe multi-walled nanotubes. Molecular mechanics simulation, Physica E 133 (2021), 114779, https://doi.org/10.1016/j.physe.2021.114779.
[60] Y. Zhao, D.G. Truhlar, The M06 suite of density functionals for main group thermochemistry, thermochemical kinetics, noncovalent interactions, excited states, and transition elements: two new functionals and systematic testing of four M06-class functionals and 12 other functionals, Theor. Chem. Acc. 120 (2008) 215–241, https://doi.org/10.1007/s00214-007-0310-x.
[61] R. Dovesi, A. Erba, R. Orlando, C.M. Zicovich-Wilson, B. Civalleri, L. Maschio, M. Rerat, S. Casassa, J. Baima, S. Salustro, B. Kirtman, Quantum-mechanical condensed matter simulations with CRYSTAL, WIREs Comput. Mol. Sci. 8 (2018), e1360, https://doi.org/10.1002/wcms.1360.
[62] R. Dovesi, V.R. Saunders, C. Roetti, R. Orlando, C.M. Zicovich-Wilson, F. Pascale, B. Civalleri, K. Doll, N.M. Harrison, I.J. Bush, P. D'Arco, M. Llunell, M. Causà, Y. Noël, L. Maschio, A. Erba, M. Rerat, S. Casassa, CRYSTAL17 User's Manual, University of Turin, Torino, Italy, 2018.
[63] D.V. Oliveira, J. Laun, M.F. Peintinger, T. Bredow, BSSE-correction scheme for consistent Gaussian basis sets of double- and triple-zeta valence with polarization quality for solid-state calculations, J. Comput. Chem. 40 (2019) 2364–2376, https://doi.org/10.1002/jcc.26013.
[64] J. Heyd, J.E. Peralta, G.E. Scuseria, R.L. Martin, Energy band gaps and lattice parameters evaluated with the Heyd-Scuseria-Ernzerhof screened hybrid functional, J. Chem. Phys. 123 (2005), 174101, https://doi.org/10.1063/1.2085170.
[65] H.J. Monkhorst, J.D. Pack, Special points for Brillouin-zone integrations, Phys. Rev. B 13 (1976) 5188–5192, https://doi.org/10.1103/PhysRevB.13.5188.
[66] S. Grimme, J. Antony, S. Ehrlich, H. Krieg, A consistent and accurate ab initio parametrization of density functional dispersion correction (DFT-D) for the 94 elements H-Pu, J. Chem. Phys. 132 (2010), 154104, https://doi.org/10.1063/1.3382344.
[67] A. Kuhn, A. Bourdon, J. Rigoult, A. Rimsky, Charge-density analysis of GaS, Phys. Rev. B 25 (1982) 4081–4088, https://doi.org/10.1103/PhysRevB.25.4081.
[68] K. Cenzual, L.M. Gelato, M. Penzo, E. Parthe, Inorganic structure types with revised space groups. I, Acta Crystallogr. B 47 (1991) 433–439, https://doi.org/10.1107/S0108768191000903.
[69] M. Julien-Pouzol, S. Jaulmes, M. Guittard, F. Alapini, Monotellurure de gallium, GaTe, Acta Crystallogr. B 35 (1979) 2848–2851, https://doi.org/10.1107/S0567740879010803.
[70] U. Schwarz, H. Hillebrecht, K. Syassen, Effect of hydrostatic pressures on the crystal structure of InS, Z. Kristallogr. 210 (1995) 494–497, https://doi.org/10.1524/zkri.1995.210.7.494.
[71] P.G. da Costa, R.G. Dandrea, R.F. Wallis, M. Balkanski, First-principles study of the electronic structure of γ-InSe and β-InSe, Phys. Rev. B 48 (1993), 14135, https://doi.org/10.1103/PhysRevB.48.14135.
[72] J.H.C. Hogg, H.H. Sutherland, Indium telluride, Acta Crystallogr. B 32 (1976) 2689–2690, https://doi.org/10.1107/S056774087600856X.
[73] D.J. Late, B. Liu, H.S.S.R. Matte, C.N.R. Rao, V.P. Dravid, Rapid characterization of ultrathin layers of chalcogenides on SiO_2/Si substrates, Adv. Funct. Mater. 22 (2012) 1894–1905, https://doi.org/10.1002/adfm.201102913.
[74] Y. Fan, M. Bauer, L. Kador, K.R. Allakhverdiev, E.Y. Salaev, Photoluminescence frequency up-conversion in GaSe single crystals as studied by confocal microscopy, J. Appl. Phys. 91 (2002) 1081–1086, https://doi.org/10.1063/1.1421215.
[75] S. Pal, D.N. Bose, Growth, characterisation and electrical anisotropy in layered chalcogenides GaTe and InTe, Solid State Commun. 97 (1996) 725–729, https://doi.org/10.1016/0038-1098(95)00608-7.
[76] P. Kushwaha, A. Patra, E. Anjali, H. Surdi, A. Singh, C. Gurada, S. Ramakrishnan, S. S. Prabhu, A.V. Gopal, A. Thamizhavel, Physical, optical and nonlinear properties of InS single crystal, Opt. Mater. 36 (2014) 616–620, https://doi.org/10.1016/j.optmat.2013.10.046.
[77] A. Chevy, A. Kuhn, M.-S. Martin, Large InSe monocrystals grown from a non-stoichiometric melt, J. Cryst. Growth 38 (1977) 118–122, https://doi.org/10.1016/0022-0248(77)90381-5.
[78] M.P. Pardo, J. Flahaut, Sur une nouvelle forme de GaS, rhomboédrique 3R métastable. Formation et étude structural (Fr.), Mater. Res. Bull. 22 (1987) 323–329, https://doi.org/10.1016/0025-5408(87)90048-1.
[79] M. Damnjanović, I. Milošević, Line Groups in Physics. Theory and Applications to Nanotubes and Polymers, Springer, Berlin - Heidelberg, 2010.
[80] M. Damnjanović, B. Nicolić, I. Milošević, Symmetry of nanotubes rolled up from arbitrary two-dimensional lattices along an arbitrary chiral vector, Phys. Rev. B 75 (2007), 033403, https://doi.org/10.1103/PhysRevB.75.033403.
[81] R.A. Evarestov, Theoretical Modeling of Inorganic Nanostructures. Symmetry and Ab Initio Calculations of Nanolayers, Nanotubes and Nanowires, second ed., Springer, Berlin - Heidelberg, 2020 https://doi.org/10.1007/978-3-030-42994-2.
[82] F. Pascale, C.M. Zicovich-Wilson, F. Lopez, B. Civalleri, R. Orlando, R. Dovesi, The calculation of the vibration frequencies of crystalline compounds and its implementation in the CRYSTAL code, J. Comput. Chem. 25 (2004) 888–897, https://doi.org/10.1002/jcc.20019.
[83] T. Lorenz, D. Teich, J.-O. Joswig, G. Seifert, Theoretical study of the mechanical behavior of individual TiS_2 and MoS_2 nanotubes, J. Phys. Chem. C 116 (2012) 11714–11721, https://doi.org/10.1021/jp300709w.
[84] V.V. Porsev, A.V. Bandura, R.A. Evarestov, Ab initio modeling of helically periodic nanostructures using CRYSTAL17: a general algorithm first applied to nanohelicenes, Comput. Mater. Sci. 203 (2022), 111063, https://doi.org/10.1016/j.commatsci.2021.111063.
[85] A.V. Bandura, S.I. Lukyanov, R.A. Evarestov, D.D. Kuruch, Calculation of young's modulus of MoS_2-based single-wall nanotubes using force-field and hybrid density functional theory, Phys. Solid State 60 (2018) 2551–2558, https://doi.org/10.1134/S1063783418120065.